



Failure of Marmolada Glacier (Dolomites, Italy) in 2022: Data-based back analysis of possible collapse mechanisms as related to recent morpho-climatic evolution and possible trigger factors

5 Roberto G. Francese^{1,2}, Roberto Valentino¹, Wilfried Haeberli³, Aldino Bondesan^{4,5}, Massimo Giorgi²,
Stefano Picotti², Franco Pettenati², Denis Sandron², Gianni Ramponi⁶, and Mauro Valt⁷

¹Department of Chemistry, Life Sciences and Environmental Sustainability, University of Parma, Parma, 43124, Italy

²National Institute of Oceanography and Applied Geophysics – OGS, Sgonico, 34010, Italy

³Department of Geography, University of Zurich, Zurich, 8057, Switzerland

⁴Department of Historical and Geographic Sciences and the Ancient World, University of Padova, Padova, 35122, Italy

10 ⁵Department of Military Geography, University of Stellenbosch, Stellenbosch, 7602, South Africa

⁶Department of Engineering and Architecture, University of Trieste, Trieste, 34127, Italy

⁷Environmental Protection Agency of Veneto, Centro Valanghe di Arabba, Arabba, 32020, Italy

Correspondence to: Aldino Bondesan (aldino.bondesan@unipd.it)

Abstract. A small, isolated portion of the Marmolada glacier partially broke off on July 3, 2022. The detached ice mass had
15 an estimated volume of 70,400 m³ and slid down the slope killing 11 mountaineers after having travelled for approximately
2.3 km along the northern slope. This event is considered among the deadliest ice avalanches historically recorded in the
Alps. The cause of the collapse is most likely to be closely related to anomalously high air temperatures in late spring and
early summer of that year and also to progressive warming of basal ice layers and subglacial permafrost. Increased melting
resulted in significant amounts of water that could not be discharged but remained trapped in crevasses of the isolated, cold
20 ice body. The usually high permeability of karst systems in limestone are likely to have been blocked by subglacial and
surrounding permafrost rocks, thereby increasing basal water pressure. Morpho-climatic data, satellite and aerial images and
geophysics were analysed to better understand role and interaction of the controlling factors. This enabled the
implementation of a conceptual model that was further investigated through numerical simulations using the Limit
Equilibrium Method. The outcome from the back-analysis indicates that a combination of driving forces was required to
25 finally trigger the collapse. The seasonal alternation of prolonged heating and refreezing meltwater of subglacial permafrost
(i.e. the active layer) could have caused the plasticization of the basal ice resulting in the presence of a “weak bottom layer”
where the available shear strength progressively dropped, finally triggering the failure.

1 Introduction

30 The catastrophic collapse of the Marmolada Glacier (Dolomites, Italy) fits into the broader worldwide context of mountain
glaciers that are experiencing unprecedented rates of retreat associated with climate change (Hock et al., 2019; Marzeion et
al., 2020; Pelto, 2020; Marta et al., 2021; Rounce et al., 2023; Zemp et al., 2019). Alpine glaciers retreat has markedly



35 accelerated since the late 1980s (Haeberli and Hoelzle, 1995; Paul et al., 2004; Zemp et al., 2015), with collapse events increasing in frequency since the early 2000s (Chiarle et al., 2022). This acceleration has further been enhanced by rapid feedback effects, as the degradation of permafrost (permanently-frozen ground) occurring at a global scale (e.g., Biskaborn et al., 2019; Rossi et al., 2022), which plays an increasingly important role on the stability of glaciers (e.g., Allen et al., 2022; Noetzli and Gruber, 2009). The phenomenon extends to the Antarctic Peninsula, where major ice shelves are collapsing due to the acceleration and thinning of feeding glaciers (Zhao et al., 2017). In the Northern Hemisphere, Greenland's glaciers are experiencing an increase in gigaton-sized iceberg-calving events, further accelerating mass loss from the Greenland Ice Sheet (Greene et al., 2024) while Himalayan glaciers are increasingly reducing their mass (Bolch et al., 2012).

40 This rapid mass loss has triggered a related increase in the frequency and magnitude of glacial collapse events (Alean, 1985; Dutto et al., 1991; Margreth et al., 2011; Gilbert et al., 2015; Lützow et al., 2023) that could be really harmful (Tian et al., 2017). The massive failure at Juuku pass in Kyrgyzstan, on July 9, 2022, involved an ice volume three times larger than the Marmolada case (Gascoïn and Berthier, 2023) and fortunately occurred in an uninhabited landscape. Similar events are documented in other regions such as the French Alps (Vincent et al., 2015; Bodin et al., 2017), the Central Andes of
45 Argentina (Falaschi et al., 2019) or the Tibetan Plateau (Zhao et al., 2022). In Switzerland, the increased frequency of collapse events in retreating glaciers is attributed to ice thinning and reductions in glacier-longitudinal ice flux (Egli et al., 2021). In the Aosta Valley, in the Italian Western Alps, and in many other alpine regions, the significant glacier retreat and the neo-formation of glacial and subglacial lakes is posing potential risks such as outbursts and floods (Aggarwal et al., 2016; Haeberli et al., 2017; Huggel et al., 2002; Viani et al., 2020).

50 Icefalls and particularly rock-ice avalanches (Noetzli et al., 2006; Bessette-Kirton and Coe, 2020; Chiarle et al., 2021) instantly release a large amount of energy, often without evident or with very few warning signs. Therefore, it is important to understand the causes that drive glacial instability to ensure better protection for downstream infrastructure and communities threatened by these severe hazards (Margreth et al., 2011; 2017).

55 Rock, rock-ice and ice avalanches from steep and cold mountain slopes often start from detachment zones affected by permafrost and cold or polythermal ice partially or totally frozen to its bed. These aspects can involve complex, climate-related thermo-hydraulic interactions (Haeberli et al., 2004a; Margreth et al., 2017), which must be considered in integrative hazard analyses and assessments (Allen et al., 2022).

60 Despite the growing body of research on glacial collapses (Haeberli et al., 2004b; Pralong and Funk, 2006; Faillettaz et al., 2011), significant gaps remain in our knowledge regarding the interplay of various factors contributing to instability. In addition the variables controlling ice avalanche rheology are poorly known (Hutter, 1997; Faillettaz et al., 2015; Thibert et al., 2018).

This study aims to partly address this gap by focusing on the catastrophic collapse of a portion of the upper Marmolada Glacier resulting in a devastating landslide that claimed several lives on July 3, 2022 (Chiarle et al., 2022; Olivieri and Bettanini, 2022; Bondesan and Francese, 2023). Variables such as permafrost degradation (Noetzli and Gruber, 2009; Rossi et al., 2022) and ice temperature probably played a primary role concerning the changing conditioning or predisposition and
65



70 final triggering of the collapse. Presumably cold ice was surrounded by rocks in permafrost conditions and the top layer of permafrost, subject to seasonal thawing and freezing (i.e., the active layer) increased significantly during the anomalous summer of 2022. This occurrence affected several variables thus requiring the development of a comprehensive digital database (see Supplementary Material for details) for better understanding the collapse. The database comprises a wide range of glaciological and meteorological records, along with historical and modern topographic maps, aerial and satellite imagery, geophysical surveys, and geological and geomorphological data collected and catalogued over the past two decades (Bondesan and Francese, 2023). The extent to which different factors contributed to the collapse can be evaluated by jointly analysing all this data providing valuable insights in understanding of glacier instability in a changing climate scenario.

75 There are few papers dealing with numerical simulation of glacial collapses (Jouvet et al., 2011; Logan et al., 2017; Löfgren et al., 2023) mostly due to the difficulties of inferring the appropriate physical and mechanical parameters of the ice and of the ice-bedrock ensemble and secondly because of the relatively rare occurrence of such events. The complex relationship between frictional sliding, water infiltration and tensional cracking (Faillettaz et al., 2011; Stearns and Van Der Veen, 2018) affects the effectiveness of deterministic approaches focused on forecasting hazards (Faillettaz et al., 2015).

80 We report here about a data-based back-analysis approach to infer the basal properties of the failure surface and get insight on the Marmolada collapse. Numerical simulations were conducted by means of the Limit Equilibrium Method (LEM), which is routinely used for slope stability analyses (Saim and Kasa, 2023) in geotechnical engineering. Particular attention was given in defining geometry and physical properties of the ice body, especially for those characterizing the interactions with the surrounding materials at the ice-rock interface. The purpose was achieved by re-processing and carefully analysing both existing and post-failure RES (Radio-Echo Sounding) profiles (Fretwell et al., 2013; Francese et al., 2019), which 85 contributed to the conceptualization of the model for numerical simulations.

By analysing changes in the glacier's geometry, surface features, and surrounding meteorological conditions, we aim to identify the controlling factors that contributed to its failure. We investigated diverse combinations of processes that may have led to glacier instability and collapse, including factors such as ice fracturing, basal lubrication, and subglacial water pressure. The complex interactions between the glacier's base and the underlying bedrock are also discussed. The factors 90 addressed include basal temperature, water content, bedrock properties, permafrost, and till distribution, all of which had a significant impact on glacier stability.

The overall structure of the paper could be outlined as follows: Section 2 provides information on the morphology and glaciology of the Marmolada massif; Section 3 describes the various data types considered for the study along with the different processing methods; The results section 4 examines the temporal and spatial evolution of the factors responsible for the collapse and introduces the outcome of the numerical simulations used to evaluate the glacier stability; Finally, an ample 95 discussion is provided in section 5 on the importance of the various factors; their complex mutual relationships are modelled in the numerical simulations.



2 General Settings

The Marmolada Glacier (ID 941, Italian Glacier Inventory) represents a prominent location within the Dolomites in northeastern Italy ($46^{\circ}26'32''$ N, $11^{\circ}51'53''$ E). This glacier drapes the northern flanks of the Marmolada massif (Fig. 1), the Dolomites' highest peak, reaching an elevation of 3343 m above sea level (asl). The signature of glacial landform shaping is clearly evident in the region (Carton et al., 2017). The underlying bedrock consists primarily of Ladinian limestone (Antonelli et al., 1990; Bosellini, 1996). The slope exposed to the North is in permafrost condition (Boeckli et al., 2012) and this is also confirmed by the temperature data collected at various depths in the nearby Piz Boè borehole. The Marmolada massif was designated a UNESCO World Heritage Site in 2009.

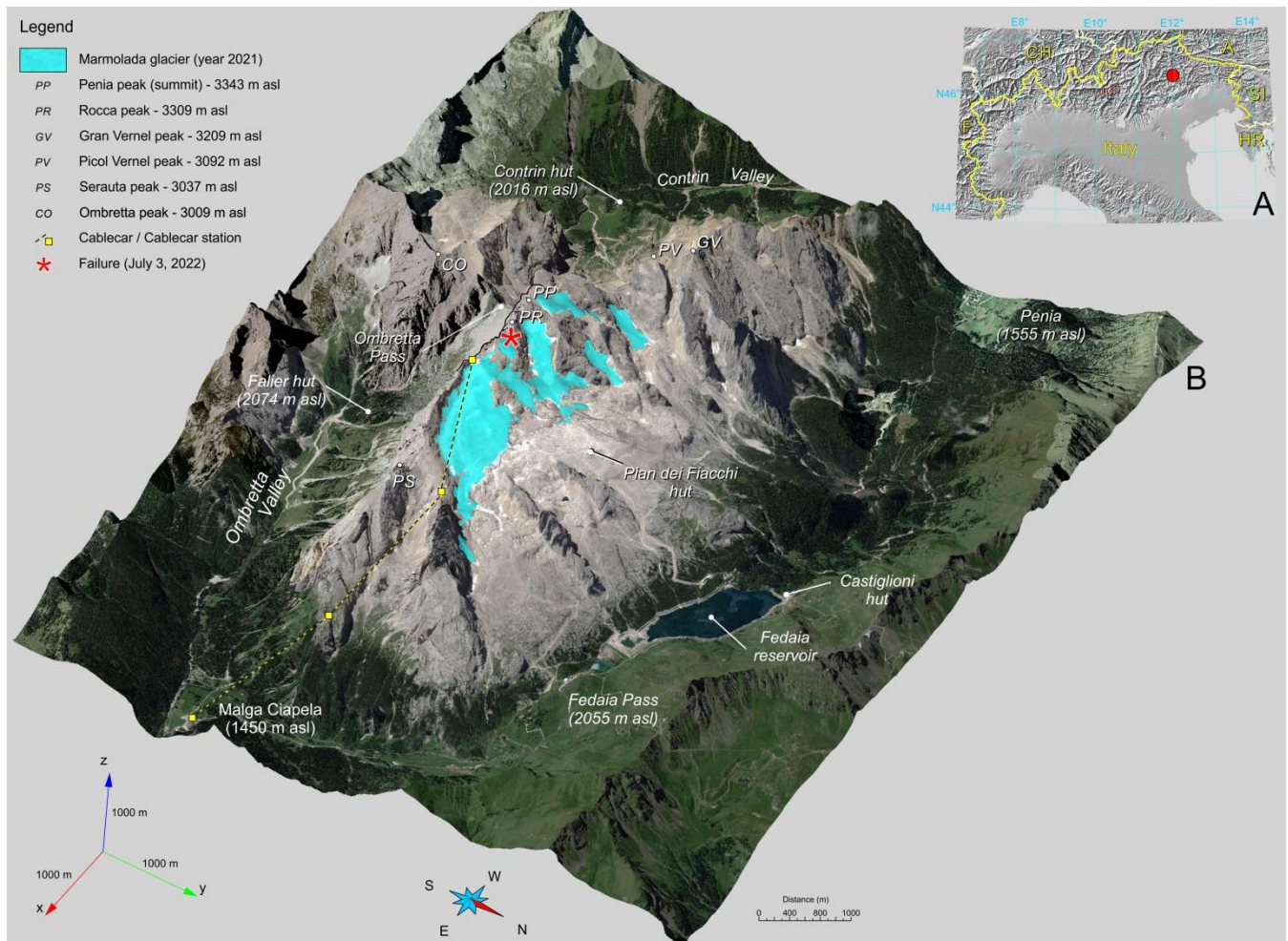
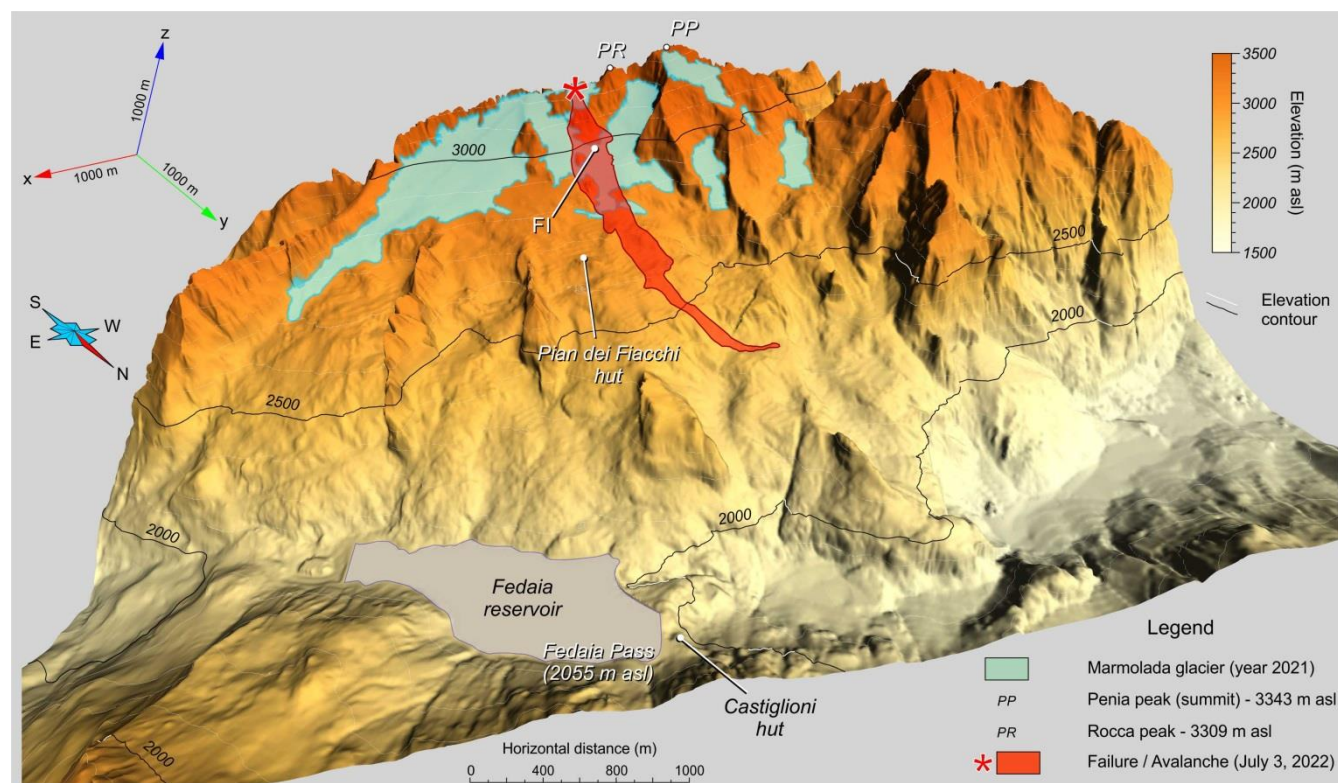


Figure 1: (A) Alpine chain with marked position of the Marmolada glacier in the north-eastern Alps in Italy. (B) Orthomosaic of satellite and aerial images of the Marmolada massif draped on a 5m by 5m digital terrain model. The lettering mark topographic and anthropic features. The failure site is marked with a red asterisk. Imagery credits: Pléiades Neo, AIRBUS Defence & Space.



2.1 The glacier

The glacier exhibits a well-documented history of retreat, particularly accelerating in recent decades following the conclusion of the Little Ice Age – LIA (Bondesan and Francese, 2023; Crepaz et al., 2013; Santin et al., 2019). This retreat has resulted in the fragmentation of the glacier into distinct sectors, with the Main Glacier (ID 941: CGI-CNR, 1962) representing the central unit. The Punta Penia Glacier (ID 941.2) flanks the massif's highest peak to the north, while the Central Glacier (ID 941.1) lies below Punta Penia.



120 **Figure 2: DTM of the Marmolada massif at the time of failure showing the flow path of the ice avalanche which extended from 3213 m asl to 2300 m asl. FI indicates the position of the first vertical impact of the collapsed mass on the lower glacier surface. The ice avalanche was only 250 meters away from the hut "Pian dei Fiacchi", which was already destroyed by a snow avalanche in 2020.**

A comparison of glacier inventories highlights the dynamic nature of the Marmolada glacial system. The 1962 inventory (CGI, 1962) identified up to eight glaciers within the massif. Subsequent years, however, witnessed significant changes, including the disappearance of some glaciers and the fragmentation of others. The most recent inventory (Smiraglia and Diolaiuti, 2016) streamlined the number of glacial units to seven and implemented revisions to their boundaries. The collective glacial front currently extends nearly 3 km.



130 It is worth highlighting that during World War I (WWI) the Alpine glaciers offered sufficient thickness to accommodate tunnels and subterranean defenses, with the Marmolada Glacier housing about 300 Austro-Hungarian soldiers (Bondesan et al., 2015). By 2004, the maximum glacier thickness had already diminished to around 45 m, while other glaciers experienced even more drastic reductions (Pasta et al., 2005).

2.2 The 2022 collapse

135 The collapse in the early afternoon of 3 July 2022 occurred at an altitude of approximately 3200 m and affected a small, isolated glacier or glacieret located in a small cirque just below Punta Rocca (3309 m asl). This massive ice body was about 160 m wide, 140 m long and 30° steep when it collapsed. The failure occurred along a large median traverse crevasse and the detachment area was shaped like a rectangle of 70 m by 90 m leaving an overhanging ice wall of about 23 m (Bondesan and Francese, 2023). The failed mass ran over the normal route to the summit (Punta Penia – 3343 m asl), overwhelming many of the mountaineers climbing at that time and resulting in 11 people killed and seven severely injured. The avalanche reached a maximum speed of 80-90 km/h and traversed 2.3 km (Fig. 2) before ending in a lateral valley at an elevation of 140 2330 m asl. At the time of the collapse, crevasses were completely water-filled and approximately 11,000 m³ of water were suddenly discharged with the failed mass (Bondesan and Francese, 2023). The flowing mass along its travel path discharged the subglacial till and also the loose glacial debris that had been deposited at the front in recent decades. A cloud of droplets, fine ice crystals, ice fragments, and debris, forming the flowing mass, widened over a front larger than 500 m and covered a surface area of approximately 350,000 m². The event was recorded by the seismic network and the resulting magnitude could 145 be estimated as 0.6 ± 0.3 .

3 Data, methods and concept

The multi-disciplinary approach of the present study involves several research topics and different data types along with the specific methods of data acquisition, analysis and processing. Predisposing and triggering factors, as well as the July 2022 failure were analysed and discussed by aid of:

- 150 - meteorological time series (temperature, rain/snowfall, snow thickness);
- permafrost and ice temperature data;
- aerial and satellite imagery;
- aerial and terrestrial laser scan measurements,
- active and passive geophysics,
155 - glaciological and geomorphological observations.

Major predisposing factors included: bedrock inclination, morphology of the niche hosting the glacieret; overall evolution of glacier and permafrost distribution in the Marmolada massif; englacial water network; progressive weakening of the ice body caused by crevasses.



Short-term conditioning or predisposition and final triggering factors may predominantly relate to the anomalously high air temperatures during late spring and early summer of the year 2022, combined with the blocking of subglacial drainage by permafrost. As a result, a significant water production by progressive intensification of surface melt, accumulated inside the cold ice body of the glacieret. This effect of prolonged heating must be seen in relation to longer-term conditioning/predisposition aspects such as the thawing and refreezing of the ground active layer, combined with changing of the plasticity conditions of a thin, basal ice layer located close to the ice-bedrock interface.

165 **3.1 Historical glacier evolution and recent meteorological and glaciological data**

Time-lapse reconstruction of the glacier geometry (1888-2021) was based on high-resolution geophysical mapping of the subglacial bedrock and on digital processing of historical and modern maps along with analysis and processing of aerial and satellite images and finally, for the recent models, using light detection and ranging (LIDAR) and terrestrial laser scan (TLS) data. Calculations were carried out using 5 m by 5 m meshes for both the glacier top and bottom. A total of 12 triplets “area, surface-area, volume” could be calculated from the set of available data. Volume error estimates range from a maximum of 25% in the year 1888 to a minimum of 7% in the year 2021. A comprehensive summary of the used data is listed in the Supplementary Material along with the computational error theory.

Available meteorological data were processed to compute yearly and monthly averages for the reference period 1900-2020 and for the year 2022. Nine weather stations located around the Marmolada massif (see Supplementary Material for the location map) were considered to provide daily time series of air temperature (min, avg. and max), snow thickness and precipitation. Among these stations, Punta Rocca (PRC) is the closest to the failure site as it is located at 3200 m asl at a distance of approximately 400 m. Missing values were reconstructed using a variety of techniques (Bondesan and Francese, 2023). The periodical observations on the glacier front, carried out by the Italian Glaciological Committee (IGC), were also implemented in the form of yearly time series to further estimate retreat rates for the period 1985-2023.

180 **3.2 Permafrost and ice temperature data**

The permafrost information for the study area was inferred from the 25 m x 25 m model for the Alpine chain (Boeckli et al., 2012) and from the nearby borehole of the Piz Boè (PZB) equipped with operational temperature sensors since the year 2011 (Crepaz et al., 2011).

The model devised by Boeckli (2012) is based on Mean Annual Air Temperature (MAAT) of the period 1960-1990. PZB data are crucial to extend the validity of this model. The PZB borehole was drilled in 2011 at 2905 m asl, which is about 300 m lower than the failure site, on the eastern slope of the Piz Boè massif, about 8 km to the NNW.

Ice temperature estimates for the Marmolada glacier were inferred by using and updating published data (Haeberli et al., 2004a; Fischer et al., 2022). In early August 2024, a borehole (Fig. 9) was drilled in the residual ice body just above the failure scarp using a steam-based drill bit and was equipped with four temperature sensors. The sensors were located at the



190 ice-bedrock interface (at a depth of 11.5 m below the surface) and at -2.5 m, -5.5 m, -8.5 m from the ice surface respectively (Fig. 12).

3.3 Satellite imagery and Seismology

Pre- and post-event satellite images were taken by the Pléiades Neo constellation (AIRBUS Defence & Space), pansharpened, pancromatic 30 cm native GSD; 6 multi-spectral channels, 1.2 m native GSD. Pancromatic sensors span from
195 ~450 nm to ~800 nm; multispectral sensors span from ~380 nm to ~880 nm. A pre-failure shot was taken on Jun 20, 2022, h 10:06:67 GMT while two post-failure shots were taken on Jul 8, 2022, h 10:02:07 GMT and Jul 9, 2022, h 10:20:21 GMT respectively.

The resolution of each normalized band was increased by a factor 3 to enhance readability on a 4k display; a Lanczos-3 interpolation kernel was used, since it provides a good balance between visual image quality and the introduction of
200 undesired spectral components (Madhukar et al., 2013). The high frequency content of each normalized band was then enhanced by subtracting from the data the output of a linear Gaussian filter having standard deviation equal to 0.9 and a gain factor of 2. The Normalized Difference Water Index (NDWI) was finally calculated computing the difference between the NIR (Near InfraRed) and green bands (McFeeters, S.K., 1996).

The seismicity of the area was inferred analysing data provided by the NOAN - North-Eastern Alps Network of OGS (CRS,
205 2024; Rebez et al., 2024). The seismic stations are located south-east and north-west of the glacier (Fig. 13A).

The failure-generated earthquake was located using an automatic routine based on the HYPO71 algorithm (Lee & Lahr, 1975) that mostly uses logic and arithmetic resulting in high computational efficiency. Additional information was retrieved via the filter picker algorithm (Lomax et al., 2012). Event onset detection was lately refined via a detailed picking of the body wave phases (in this case P-wave only) in the records of six of the surroundings NOAN stations. The localization of the
210 event appears accurate as it corresponds to the real position with an error of about 2km (Fig. 13B) despite there being no NOAN stations in the north-east quadrant.

3.4 Geometry of the failure zone

At the collapse site, surface morphology was reconstructed immediately after the event mostly using UAV (Unmanned Aerial Vehicle) LIDAR and TLS data while the buried bedrock geometry was reconstructed using a combination of pre- and
215 post-failure geophysical profiles (Fig. 9). The residual ice surface and the outcropping bedrock were modelled using 0.05 m by 0.05 m mesh. Post-failure RES profiles were collected in October 2022 just above and around the failure edge. The profiles were collected using a Subsurface Interface Radar (SIR) 4000 equipped with 200 MHz and 500 MHz antennas (Fig. 9). Some additional scanlines, located around the failure edge, were recovered from the 2004 RES campaign (Pasta, 2004). These data required to be converted back to amplitude time series (see Supplementary Material for details) prior to be geo-
220 referenced and re-processed. Seismic Unix (Stockwell; 1999; Picotti et al., 2017) was utilized for the purpose. The buried



bedrock response was then interpolated over a 1.0 m grid. This set of RES profiles was functional to the reconstruction of the geometry and physical properties of the ice-rock interface below the failed glacieret.

3.5 Glacieret stability and back analysis

The stability of the glacieret was assessed along a representative 2D cross section by means of the Limit Equilibrium Method (LEM), which is routinely used for slope stability analyses in geotechnical engineering. LEM considers the equilibrium of a rigid body, such as the slope or the glacier in this case, along a slip surface of any shape. From this equilibrium, the driving actions are calculated and compared to the available resistance calculated according to Mohr-Coulomb's shear strength criterion. From this comparison, the Factor of Safety (FoS) is derived. FoS is the ratio between resisting and driving actions. The lower the FoS the higher the possibility of instability and collapse. If FoS is less than one, the slope is unstable and FoS = 1 is assumed as the limit stability value. Among the variety of methods of slices available to determine FoS, three different methods were used in this analysis, namely, Janbu simplified - J (Janbu et al., 1956), Janbu corrected - Jc (Janbu, 1954; 1973), and GLE/Morgenstern-Price (Morgenstern and Price, 1965).

The ice shear strength parameters (cohesion and friction angle) were inferred by the available literature. Seaki et al., (1985) conducted a multi-temporal analysis on cohesion and friction angle of sea ice over a six year period and in different temperature conditions. Tang et al., (2024) carried out direct shear tests on polycrystalline ice at temperatures ranging between -0.5 and -40 °C, obtaining Mohr-Coulomb shear strength parameters. The upper portion of the Marmolada glacier could be probably considered polythermal, at least above 3000 m of elevation (Bondesan and Francese, 2023; Boeckli et al., 2012). Similar ice temperature conditions were encountered during summer campaigns in the Ortler-Cevedale massif approximately at the same elevation (Francese et al., 2019). In addition, data from PermaNet (Crepaz et al., 2011), a long term permafrost monitoring project confirm these temperature conditions. Based on the above considerations and known ice temperatures of Alpine sites (Fig. 8B), an ice temperature ranging from -2.5°C to -4°C was selected to estimate the appropriate parameters and carry out the numerical simulations. These initial values were confirmed by borehole temperature measurements in the ice collected in August, 2024 right at the failure site (see Section 3.2).

Equivalent parameters for the Marmolada limestone were also inferred from the available literature and particularly from a systematic classification of the Dolomitic rocks (Longo, 2018) based on the RMR - Rock Mass Rating System (Bieniawski, 1989).

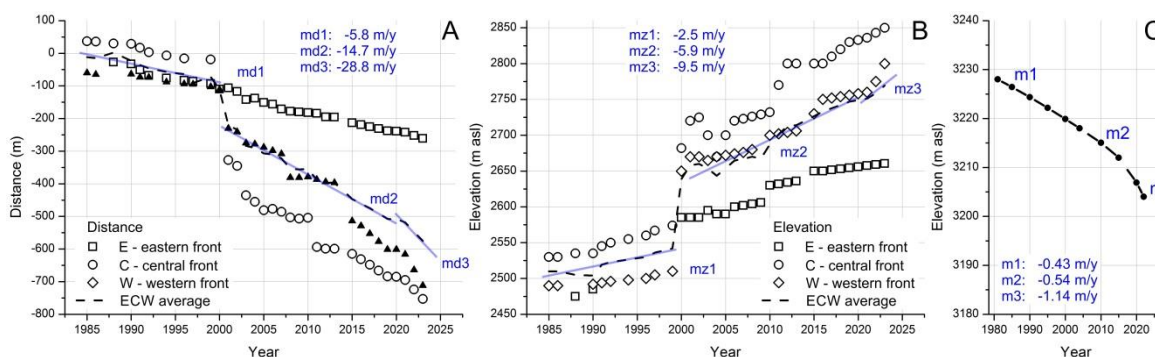
Additional and more detailed information on data and methods can be found in the Supplementary Material and in Bondesan and Francese (2023) in both the paper and the appendix.



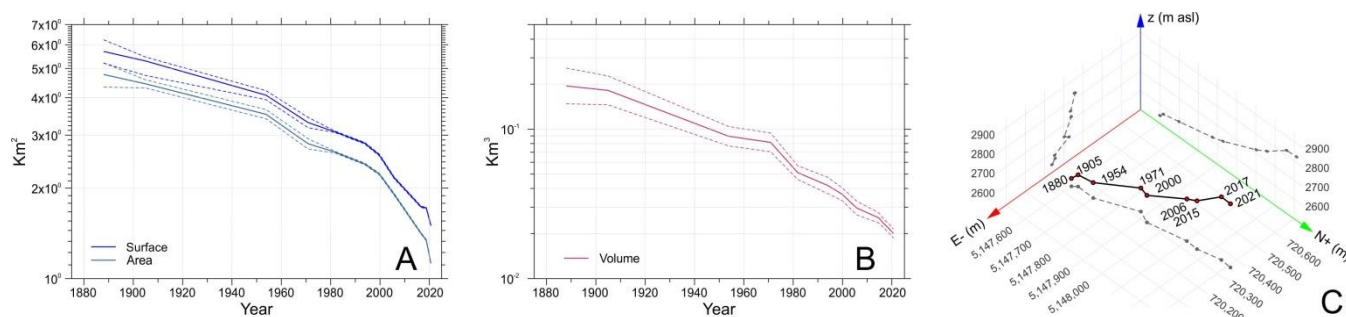
4. Results

250 4.1 Overall evolution of the Marmolada glacier

Field measurements conducted by the IGC since the early Eighties (Fig. 3A and Fig. 3B) clearly show the progress of the retreat. Distance and elevation measurements are referred to specific benchmarks located in the western, central and eastern sector respectively. Retreat in the eastern sector is not as drastic as in the central and western sectors. The averaged ~30-year trend clearly exhibits three different gradients for both distance and elevation. The sudden jump occurring in the year 2000 is caused by a partition of the glacier in correspondence with a vertical step in the outcropping bedrock. The three gradients could be also recognized in the graph reporting the lowering of the glacieret's surface (Fig. 3C) right at the failure site.



260 **Figure 3: Front migration and surface ablation measurements for the Marmolada glacier. A reference point was available for each the different glacier sections (see also Fig. SM 4). (A) Inclined distance taken from the glacier front over the period 1985-2023. (B) Vertical distance taken from the glacier front over the period 1985-2023. (C) Progressive lowering of the glacier surface in the period 1980-2022 computed right at the point of collapse.**



265 **Figure 4: Over a century (1888-2021) of retreat of the Marmolada glacier as for area, surface, volume and front migration obtained via GIS/CADD analysis and processing. (A) Area and surface reduction, the interval of confidence is represented by dashed lines. (B) Volume reduction, the interval of confidence is represented by dashed lines. (C) Tri-dimensional spatial migration of the centroid of the glacier front (the centroid was calculated as the arithmetic mean of the xyz coordinates of the nodes in the polyline representing the glacial front in different years).**



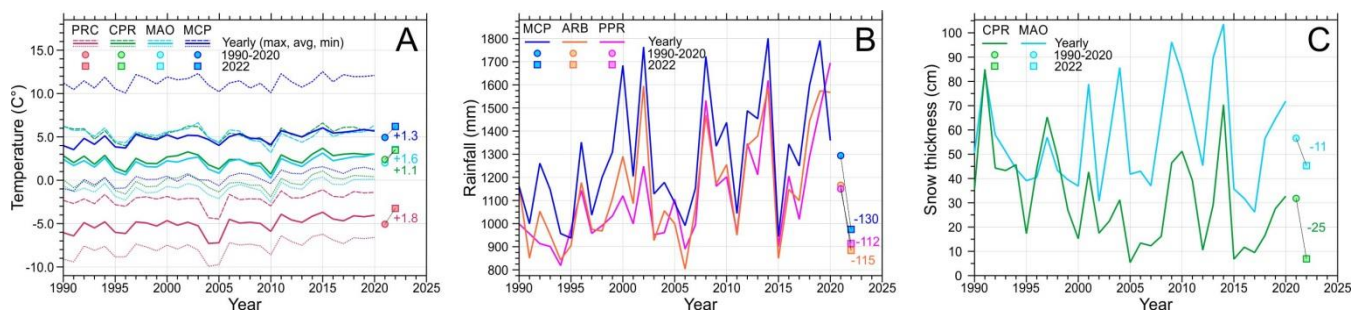
270 Area, surface and volume, computed for 12 time frames since 1888, show the longer-term retreat trend (Fig. 4A, Fig. 4B).
The space migration of the centroid of the glacial front is also a good indicator of the retreat trend (Fig. 4C). After
approximately one century (1982) the surface area was $53.9 \pm 0.7\%$ of the initial surface, while the volume was $26.2 \pm 12.5\%$
of the initial volume. In the year before the failure (2021) the surface was $26.4 \pm 0.5\%$ of the initial surface, while the volume
was $10.2 \pm 7.5\%$ of the initial volume. In a period of about 130 years the Marmolada glacier lost approximately 73% of the
275 surface area and 90% of the volume.

This overall evolution of the Marmolada glacier, in terms of surface reduction and mass balance, shows a trend similar to
that of the other European glaciers (Bondesan and Francese, 2023).

4.2 Meteorological variables and permafrost conditions

The year 2022 proved to be particularly anomalous as for temperature, rainfall/snowfall and snow cover in comparison to the
280 ~30-year period 1990-2020.

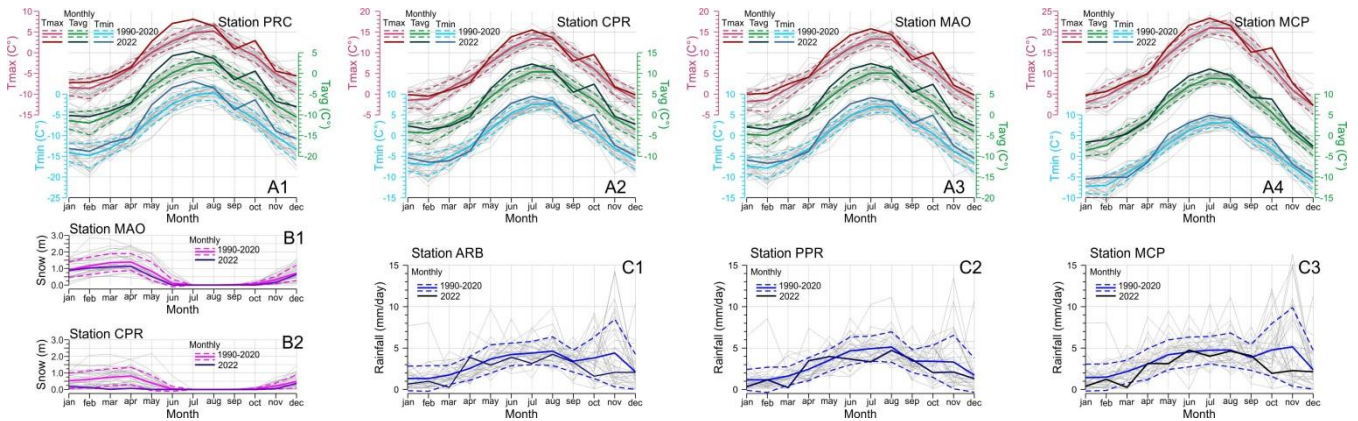
The annual temperatures for the year 2022 showed a marked positive shift in comparison with the 30-year average for the
period 1990-2020. The positive shift of average temperature (labeled avg in Fig. 5A) was $+1.8^\circ\text{C}$, $+1.1^\circ\text{C}$, $+1.6^\circ\text{C}$ and
 $+1.3^\circ\text{C}$ for the stations PRC, CPR, MAO and MCP respectively (Fig 5A). The positive shift for the station PRC is
particularly high and it is also higher considering the positive shift of the minimum value that happened to be equal to
285 $+1.9^\circ\text{C}$. Contrarily annual precipitations for the year 2022 (Fig. 5B) showed a negative shift of about 120 mm (average of
three stations) corresponding to a reduction in annual precipitations of approximately 22%. Finally considering the snow
thickness for the year 2022 (Fig. 5C), a negative shift of about 18 cm (average of two stations) was observed, corresponding
to a reduction in annual snow thickness by about 41%.



290 **Figure 5: Annual meteorological variables pertaining to the ~30-year reference period 1990-2020, see Supplementary Material for station code and position: PRC is located at 3250 m asl and it is the closest to the failure site (~400 m); in each panel is graphed: the annual curve; the ~30-year average (circle mark); the 2022 value (square mark). The numbers on the right of each panel represent the Δ between the ~30-year average and the 2022 value. (A) Minimum, maximum and average temperature curves, Δ were computed for the average values only. (B) Rain/snowfall. (C) Snow thickness. See text for further details.**

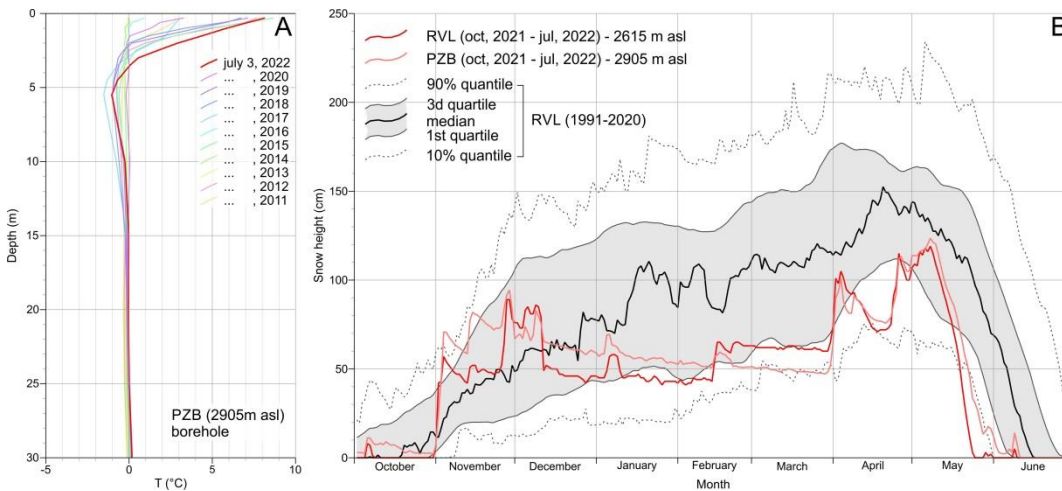
295

A more accurate analysis could be done considering the monthly time series (Fig. 6). Data from the year 2022, similarly to
yearly time series analysis, are compared to the 30-year period 1990-2020.



300 **Figure 6: Monthly meteorological variables related to the ~30-year reference period 1990-2020, see Supplementary Material for station code and position: PRC is located at 3250 m asl and it is the closest to the failure site (~400 m); in each panel is graphed: the monthly curve per each year (solid line in gray color); the ~30-year average (solid line); the standard deviation interval (dashed line); the monthly curve for the year 2022. (A) Minimum, maximum and average temperature curves. (B) Snow thickness. (C) Rain/snowfall. See text for further details.**

305 Monthly temperature averages (Fig. 6A) clearly show how during the period May-July 2022 the recorded temperatures fall outside the standard deviation range for the 30-year reference period as for minimum, average and maximum values. It is worthwhile to notice that the values recorded at the PRC station, during the year 2022, reach the absolute maxima for the period May-July (Fig. 6A1). With regard to rainfall/snowfall (Fig. 6C) the 2022 values fall within the standard deviation range for the reference period although the curve is very close to the lower bound.

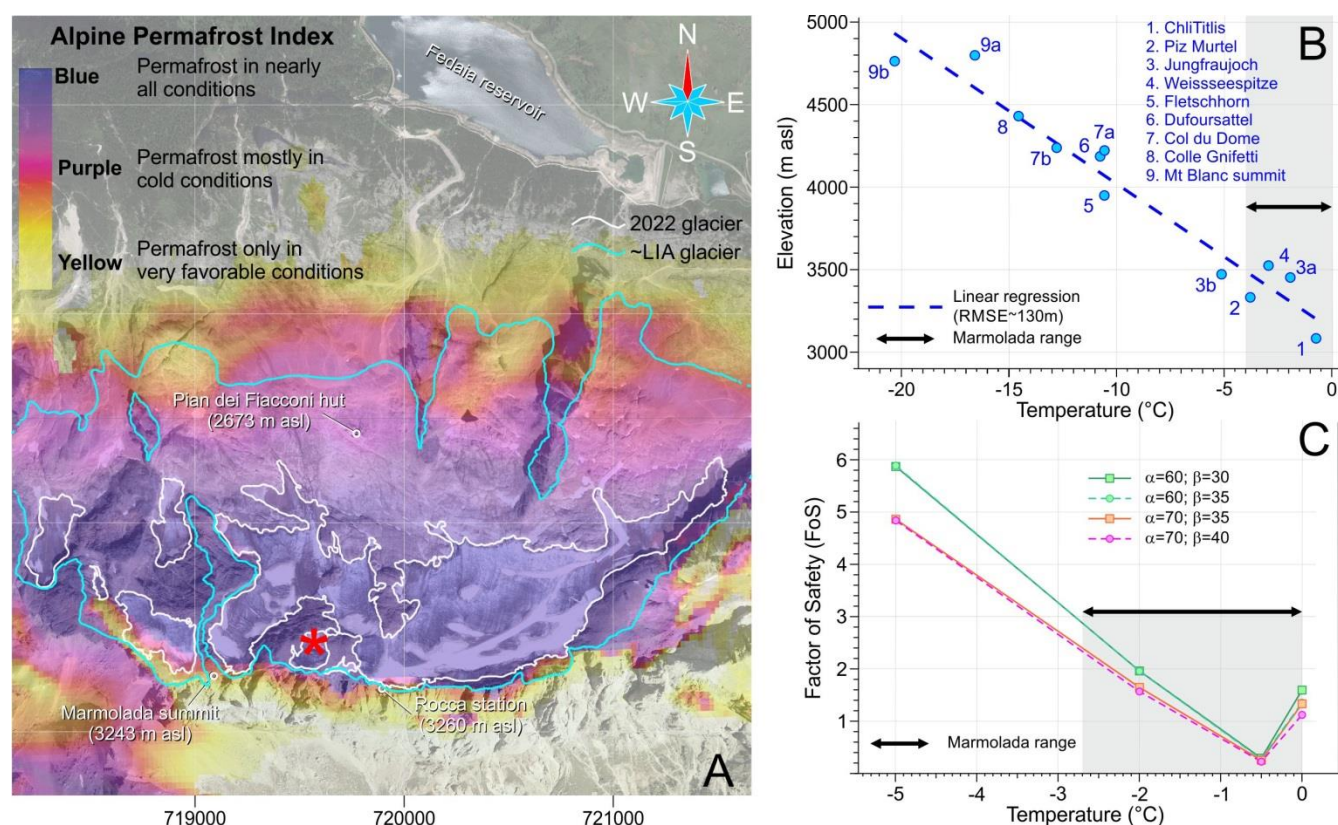


310 **Figure 7: (A) Borehole temperature measurements collected on July 3 of each year since 2011 at the PZB station (see Supplementary Material for station code and position). (B) Seasonal snow height at RVL and PZB stations in 2022 in comparison to the average snow height of the period 1990-2020 measured at the RVL station (see Supplementary Material for station code and position).**

315



Snow cover during winter and spring of the year 2022 was particularly thin (Fig. 6B). The thickness value was just below the average (Fig. 6B1) north of the Marmolada glacier (MAO station) and approximately along the lower bound of the standard deviation interval (Fig. 6B2) south of the Marmolada (CPR station).



320 **Figure 8:** (A) Modeled permafrost occurrence in the Marmolada massif (after Boeckli et al., 2012). The detachment zone is
 marked with an asterisk. A strong contrast exists between the sun-exposed, ice-free south wall with its warm, probably non-frozen
 rocks, and the cold north-slope oriented away from the sun and with widespread permafrost. The glacier boundary in July 2022 is
 325 outlined with a white line while the line in cyan color outlines the boundary of the LIA glacier. (B) Ice temperature measured at
 different sites in the Alps (redrawn from Haerberli et al., 2004a and updated including the Weissseespitze from Fischer et al., 2022).
 The guessed thermal conditions at the Marmolada detachment fit the linear regression curve. The graph is indicative as this
 temperature information is from different times and obtained with different methods/accuracies. (C) Overall stability of frozen
 rocks with ice-filled clefts as a function of rock temperature from centrifuge experiments for four sets of slope angle “ α ” and
 inclination of discontinuity “ β ” (redrawn from Davies et al., 2001). Imagery credits: Pléiades Neo, AIRBUS Defence & Space

330 Analysis of snow thickness was extended including daily time series from two additional stations (Fig. 7B) to overcome
 local variability uncertainty (exposition, wind, etc.). These stations are located a few kilometers north (PZB) and north-east
 (RVL) to the Marmolada glacier. Snow cover in the period October, 2021 – June, 2022 is compared to snow cover during the
 30-year reference period 1991-2020 recorded at the RVL station. The snow-cover curves, in the first months of the year
 2022 are way below the average and close to the 10% quantile limit for both the two stations. In early April and early May
 335 the curves enter the first quartile of the reference period but in late May the curves drop to almost zero thickness falling



below the 10% quantile. These data show clearly how in the year 2022 the snow melted one month early and that at an elevation of 3000 m asl there is very little snow left after the mid of June. The negative shift of the RVL curve depends mostly on its lower elevation.

Permafrost data were not directly measured for the Marmolada massif as there are no boreholes or other sensor installations.

340 The nearest sensor is located in a borehole (station PZB) in the Sella massif (See Supplementary Material for the location map) at an elevation of 2905 m asl (Fig. 7A) and it is operational since the year 2011 (Crepaz et al., 2011) continuously sampling the temperature. Temperature values collected in early July of each year were graphed beginning from the summer 2011. On 3 July 2011, permafrost in carbonate rocks below an active layer of about 2 meters was already near 0°C at the depth of zero annual amplitude (zaa, ~ 15 m) and below but still reached beyond 30 m, while in 2022 the permafrost base is
345 at about 25 m below the surface and the active layer is around 3 meters.

The surface temperature on July 3rd 2022 is near the maximum of this time series. The temperatures at depth close to 0°C and the near-zero temperature gradient/heat flow suggest that there is long-term warming and degradation of permafrost going on at the PZB site and in the region as it is generally characteristic for permafrost on Earth because of the ongoing global warming (Biskaborn et al., 2019). Together with the modelled permafrost occurrence (Boeckli et al., 2012; Gruber,
350 2012), this suggests that permafrost occurs around the detachment zone, although degraded, in nearly all conditions (Fig. 8A). It should be finally noted that permafrost in ice-free terrain was colder and reached lower altitudes during the LIA.

4.3 Characterization of the failure zone

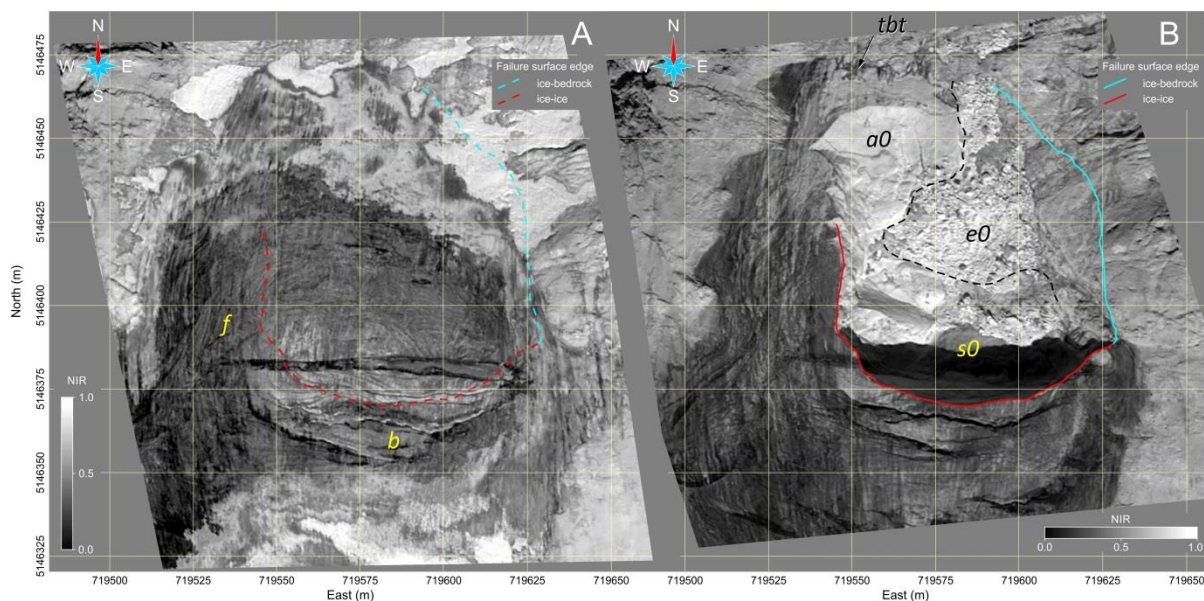
Pre- and post-failure satellite imagery provided some insight on the collapsed glacieret. Image analysis focused on the failure surface and on the water content.

355 The NIR (Near-InfraRed) map (Fig. 9A) before the failure clearly shows a highly foliated ice body with a wedge-shaped median/traverse crevasse along with a series of the rear crevasses. The median crevasse appears to be filled with water with floating ice and snow. The maximum width of the median crevasse occurs on the eastern side and it measures approximately 5 m. A narrow bédrière (a torrent running over the surface of a glacier and fed by meltwater) developed on top of one of the rear crevasses and it is oriented almost transversally to slope with its discharge to the east on the glacieret surface right at the
360 intersection with the large median crevasse. The same map after the failure (Fig. 9B) provides important details on the detachment. The area of the basal detachment surface is about 6200 m² and the rupture occurred at the boundary of three different materials: ~32% along a foliation (a0, ice-ice); ~36% nearby bedrock (s0, ice-thin ice); ~32% at the top of the bedrock (e0, ice-bedrock). The bedrock in the a1 sector is just partly visible because it is completely covered by ice/snow blocks and ice debris.

365 The NDWI (Normalized Difference Water Index) map (Fig. 10A) before the failure is mostly effective in detecting the presence of water (outlined by high values of NDWI). A bédrière-like outflow pattern is visible in correspondence to the eastern edge of the large median crevasse (marked by letter b in Fig. 10A) indicating that the crevasse is mostly water-filled

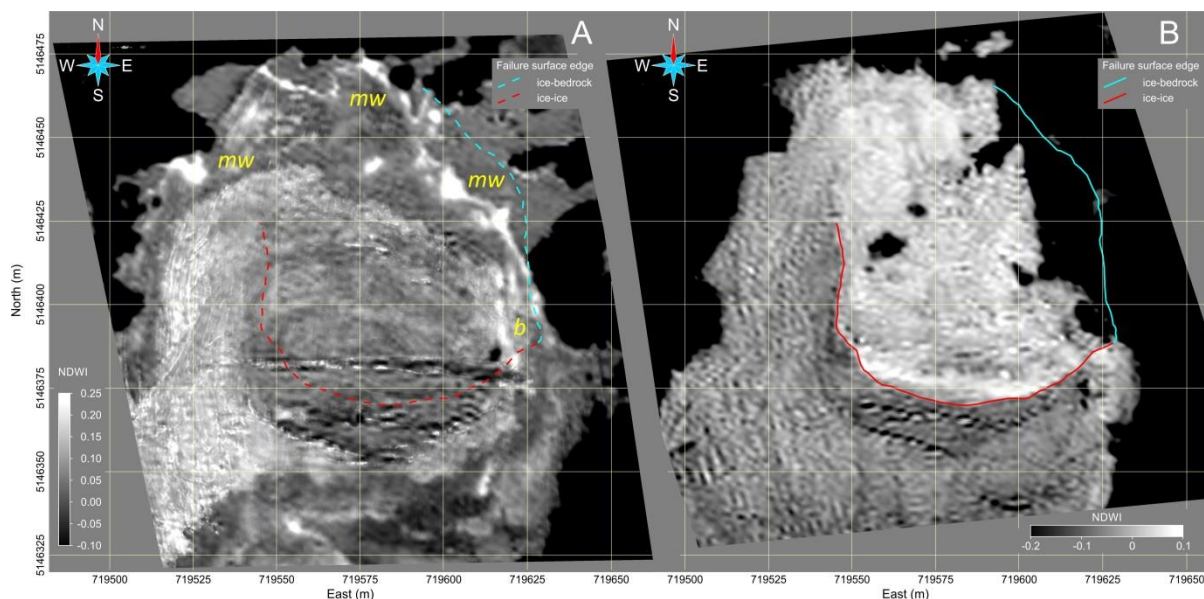


below a snow/ice plug. A high NDWI response is also visible along the edge of the various crevasses suggesting the presence of water below plugs of snow and ice.



370

Figure 9: Near-Infrared satellite images (Pléiades Neo, AIRBUS Defence & Space) of the glacieret taken before and after the failure. (A) Date of acquisition: June 20, 2022; f – foliated ice; b – transversal bédrière. (B) Date of acquisition: July 8 and July 9, 2022; a0 – relatively thick residual ice layer; s0 – exposed bedrock; e0 – thin ice layer; tbt – thin basal till. See text for details.

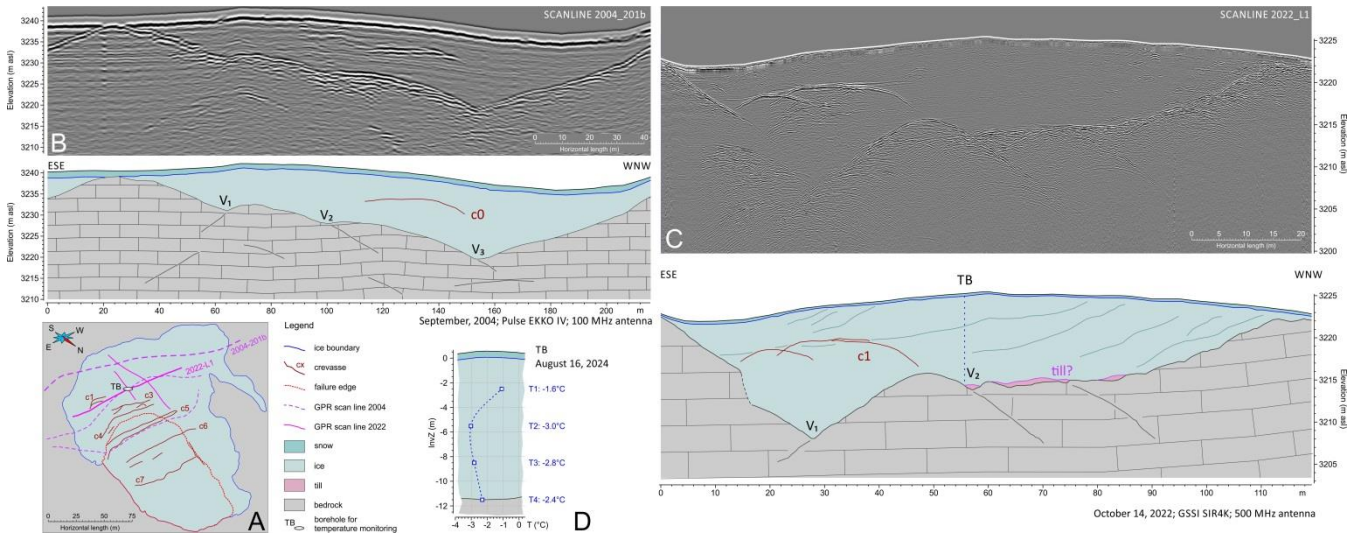


375

Figure 10: NDWI (Normalized Difference Water Index) map obtained via processing of multispectral satellite images (Pléiades Neo, AIRBUS Defence & Space) of the glacieret before and after the failure. (A) Date of acquisition: June 20, 2022; b – longitudinal bédrière; mw - meltwater. (B) Date of acquisition: June 20, 2022. See text for details.



380 Meltwater is finally visible along the snow-ice boundary and it probably accumulates because of the counter slope caused by
the snow layer. Apparently there is no water discharge at the toe of the glacieret. Very little water evidences are visible after
the failure (Fig. 10B) indicating that most of the englacial water was somehow discharged during the collapse.

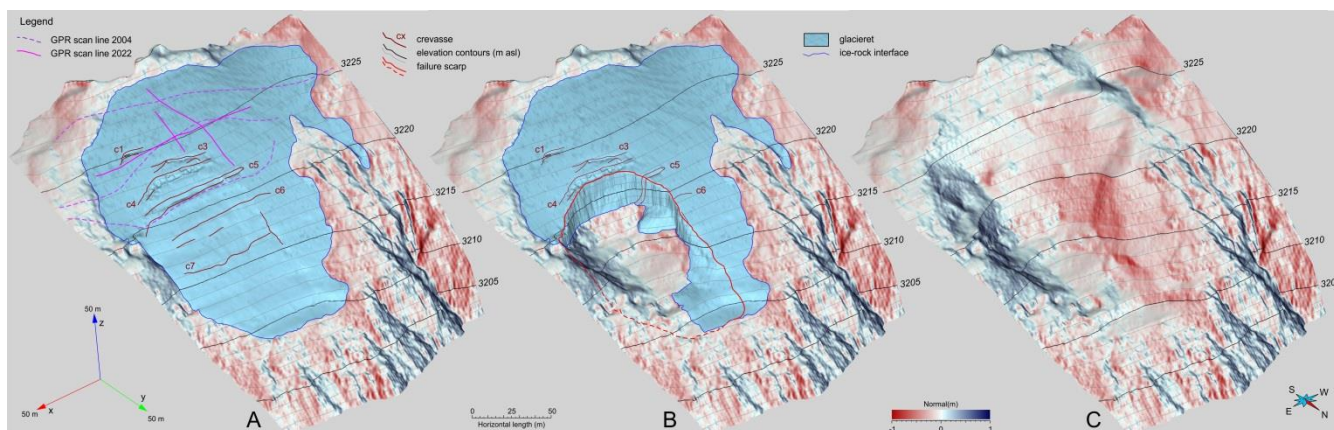


385 **Figure 11: RES profiles collected just above the failure scarp before and after the collapse. (A) Sketch map showing the location of the profiles. (B) Scanline 2004-201b (reprocessed from Pasta, 2004): data and interpretation; bedrock and crevasse response is clearly visible. (C) Scanline 2022-L1: data and interpretation; bedrock morphology is clearly imaged along with crevasses, foliations and some thin layers of anomalous response interpreted as basal tills. Troughs V_i could be correlated across the two different profiles. (D) Temperature record from the borehole measurements taken on August 16, 2024. See text for further details.**

390 RES profiles (Fig. 11A) aided in outlining the buried bedrock morphology and the ice structure above and on the side of the
failure scarp. A first profile collected several years before the failure (Fig. 11B) outlines the bedrock morphology in the
upper slope, at a distance of approximately 50 m from the failure scarp. The bedrock exhibits three incisions (V_1 , V_2 and
 V_3) with a maximum ice thickness of about 20 m at incision V_1 . The response of a crevasse (c_0), no longer present, is
visible in-between V_2 and V_3 . A second profile collected three months after the failure just above the failure scarp (Fig.
395 11C) shows similar features but with greater resolution. Two incisions are clearly visible and they nicely correlate with V_1
and V_2 of the previous profile while V_3 is just lightly engraved. High-amplitude diffraction hyperbolas mark the top of some
humps in bedrock morphology. The maximum ice thickness is about 16 m at incision V_1 . Diffractions and reflections from
crevasse c_1 are visible at the beginning of the radar profile. A series of low-amplitude and east-dipping reflectors are
embedded in the ice body. It is the response of the ice foliations described in the satellite images. Very short wavelength
400 radio waves are needed to outline these tiny reflectors. Gently east-dipping bedding planes are partly outlined by reflections
within the bedrock and the response of some fractures is also clearly visible. The profile was collected almost parallel to the
strike of the strata.



Ice foliations and rock beddings are barely detectable in the 2004 profile due to the low frequency of the radar transducer (100 MHz) while foliations are clearly imaged in the RES-scan collected in October 2022 (Fig. 11C). The foliation planes
405 apparently dip eastward, with an inclination of less than 6-7 degrees. Some low-reflectivity thin layers are visible right on top of the bedrock in the central and western segment of the 2022 RES-scan. The poor degree of reflectivity suggests the presence of a dispersive medium, typical of cohesive sediments, which could be reasonably interpreted as a basal till comprised of finely crushed rocks.



410 **Figure 12: 3D-morphology of the rock-ice ensemble modelled right at the detachment site. (A) Pre-failure settings; the volume of the glacieret is approximately 159,000 m³. (B) Immediate post-failure settings; the residual ice volume is approximately 89,000 m³. (C) Bedrock morphology reconstructed via RES imaging below the residual ice body; the bedrock niche where the glacier failed had a basal dip that ranged from 41 degrees in the rear portion to 20 degrees in the frontal part.**

415 The reconstruction of the buried bedrock morphology allowed for a precise modelling of the area of the collapse (Fig. 12). The volume of the glacieret, prior to collapse, was approximately 159,000 m³ (Fig. 12A), contained within a perimeter of ~800 m, while the collapse involved about 70,000 m³ (Fig. 12B) of ice, water and various debris leaving ~89,000 m³ of ice in-situ. The perimeter of the failed mass is about 375 m and the failure surface, including the nearly vertical faces, could be estimated at 9,700 m². The failed mass was hosted in a rock niche with a steep rear portion and a gentle frontal part. The
420 bedrock inclination is approximately 41° in the rear portion and it is less than 20° in the frontal part (Fig. 12C).

The temperature of the ice surface along the failure scarp was measured several times with airborne sensors: the early morning after the failure (7:00 AM of Jul 4, 2022; at the beginning of September (Sep 7, 2022) and in mid-October (9:00 AM of Oct 14, 2022). The maximum temperature value was -9°C in summer time and -10°C in early autumn (See Supplementary Material for details and figures).

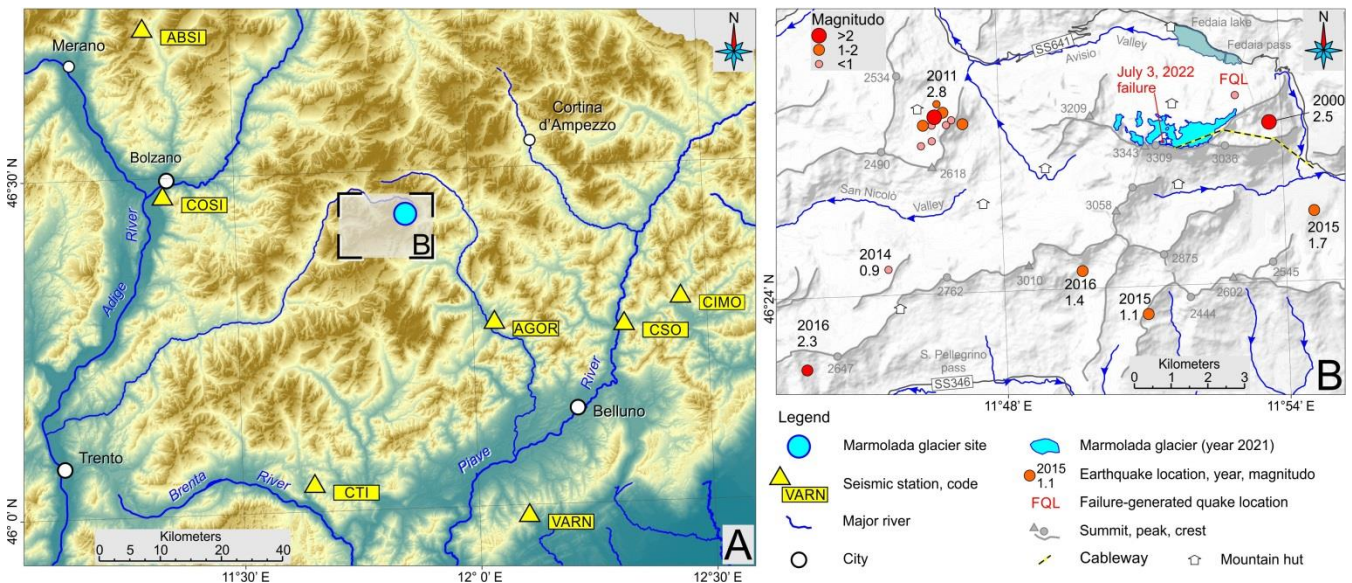
425 The post-failure exposed bedrock temperature was similarly measured in the early morning the day after the failure (M. Zumiani, personal communication): the value was below zero suggesting permafrost conditions in agreement with the Alpine model (Boeckli et al., 2012).



Following the drilling and sensor installation in August 2024, the vertical ice temperature profile was obtained two weeks later, after the thermal conditions around the borehole in the residual glacier had stabilized. The temperature at the ice-bedrock interface (-11.5 m below the ice surface) was -2.4 °C while the temperature within the ice body was of -2.8 °C, -3.1 °C and -1.6 °C at -8.5 m, -5.5 m and -2.5 m below the ice surface respectively (Fig. 11).

4.4 Seismology

Earthquakes in this area mainly occur far from the Marmolada massif. Typical earthquakes occur east and southeast of Agordo and of the Piave river along the outer front of the Southeastern Alps (Gentili et al., 2011; Sukan and Peruzza, 2011). In the last twelve years, the seismicity within 5 km of Marmolada (Fig. 13B) has been limited to a cluster south of Canazei (west of Marmolada) and a few $M < 2.5$ magnitude events, including the $M 2.5$ earthquake occurred in 2000, which is the closest event to Marmolada. The latter is located just south of Malga Ciapela. This uncertainty falls within the typical errors for seismic event location (D'Alessandro et al., 2011). An accurate positioning was then achieved minimizing the misfit of the arrival times and considering a regional velocity model devised for this area of the north-east Alpine chain.

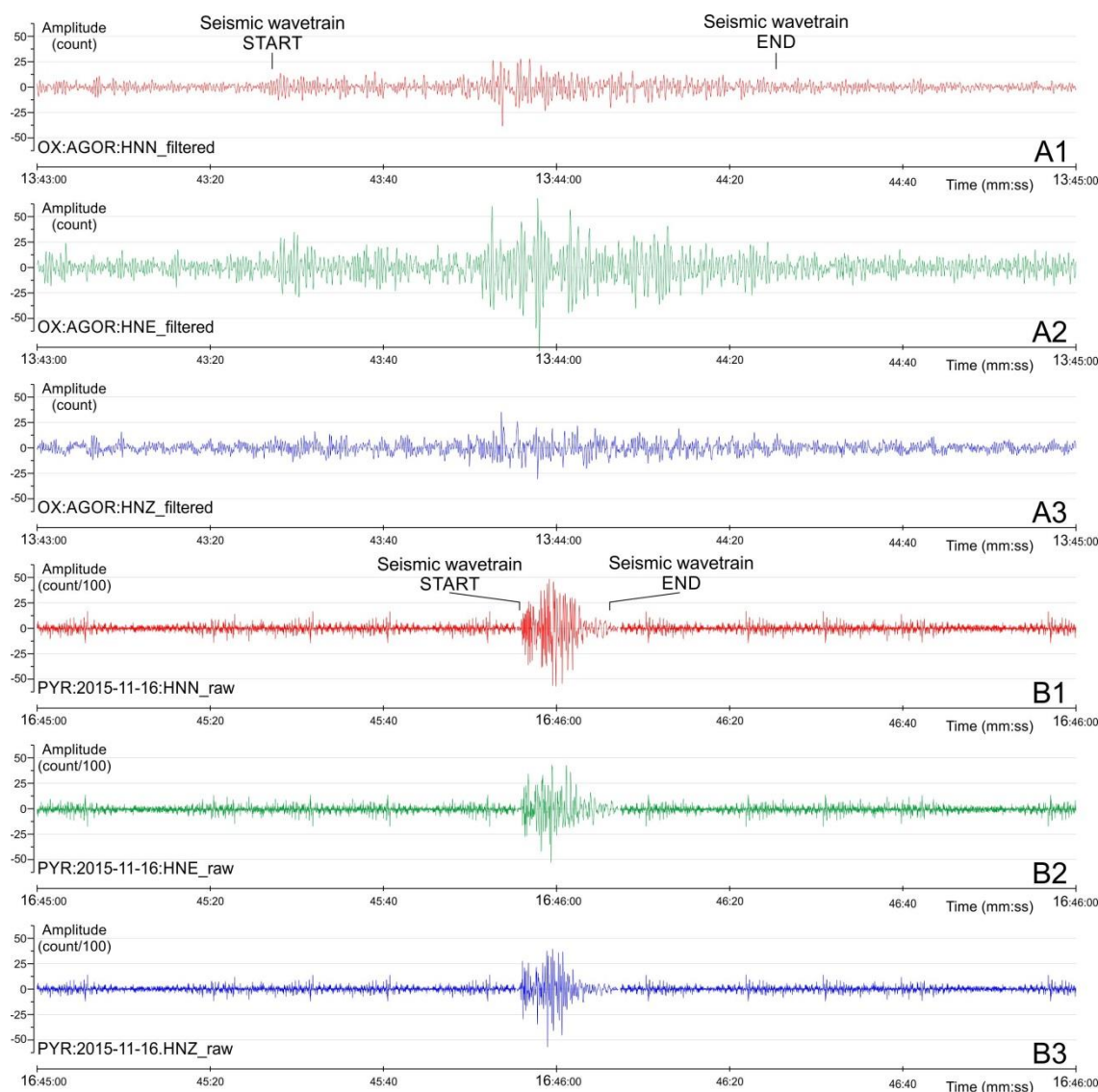


440 **Figure 13: Seismological settings. (A) Topographic map showing the location of the seismic stations around the Marmolada glacier. (B) Historical earthquakes occurred in the vicinity of the failure site; the FQL letter designates where the earthquake that was caused by failure was recorded by the nearby seismic stations; an earthquake with magnitude 2.5 was detected in the year 2000 just east of the glacier. On the day of the collapse only three earthquakes (Table 2) occurred in northern Italy and they were**
445 **located more than 50 km from the glacier.**

The seismic wavetrain generated by the glacial collapse (Fig. 14A) lasts for approximately 60 seconds and this time interval roughly corresponds with the duration of the event deduced from the various available video footages. The seismic record appears to be mostly dominated by the horizontal component of surface waves (Rayleigh and Love) with a dominant



450 frequency in the range comprised between 1.5 Hz and 5 Hz. The major amplitudes were recorded in the horizontal channels and particularly in the EW channel (Fig. 14A2). Most of the energy was released after 25-35 s since the first major impact of the avalanche on the glacier surface located 250 m below the failure zone.



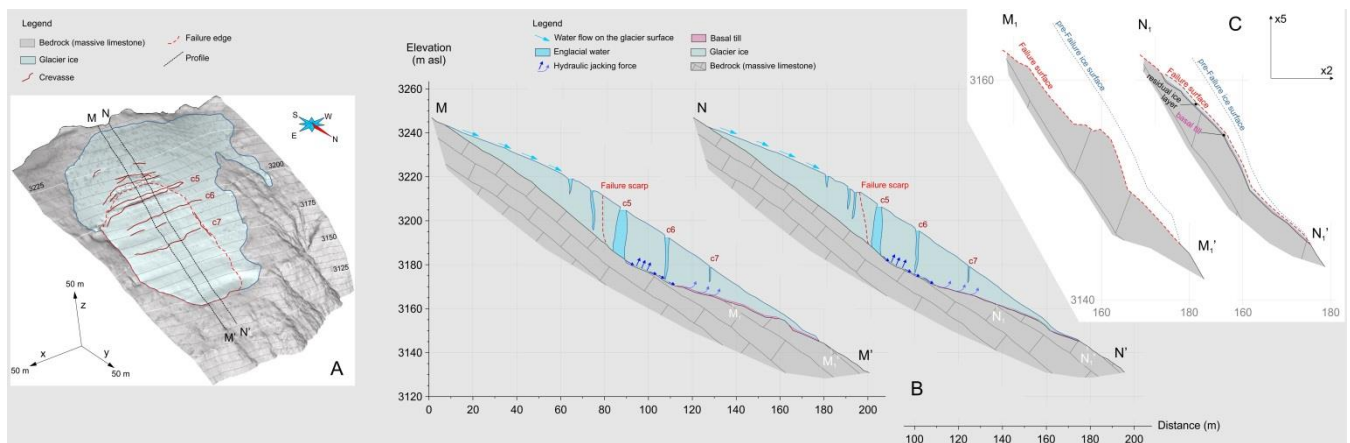
455 **Figure 14: Seismological records. (A) Time series of the horizontal (A1 and A2) and vertical (A3) components of the ground motion induced by the Marmolada failure. Surface waves dominate the recordings indicating that the rupture occurred very close to the surface thus negating the hypothesis of seismic triggering of the rupture. (B) Time series of the horizontal (B1 and B2) and vertical (B3) components of the typical ground motion caused by an ice-rock fall as recorded in the Himalaya region nearby the Everest base camp.**



460 The character of the seismic wavetrains of the Marmolada failure, as for surface waves, is particularly similar to the records
of an ice-rock avalanche recorded in the Himalaya region nearby the Everest base camp in the year 2015 (Fig. 14B). The
465 difference in the duration of the wavetrain is mostly related to the distance between the recording station and the event itself
that is approximately 22 km and 6 km in the Marmolada and Everest cases respectively.

4.5 Slope stability back analysis

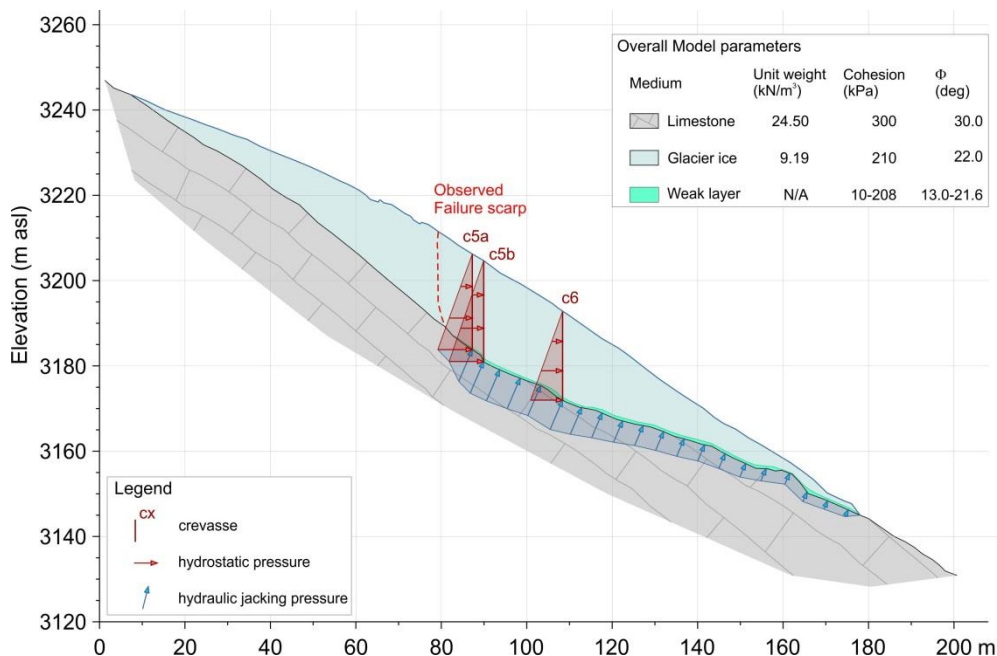
465 The comprehensive characterization of the collapse zone led to the construction of a detailed pre-failure model of the
glacieret (Fig. 15).



470 **Figure 15: (A) Pre-failure model of the glacieret with evidenced the lower transversal crevasses and the cross sections MM' and NN'. (B) Cross section MM' and NN' showing a schematization of the glacieret with indicated: failure surface; bedrock morphology; hydraulic jacking forces, etc. (C) Post-failure models of the lower portion of the failure surface along cross sections M₁M₁' and N₁N₁' (letters are indicated in panel B). The failure surface developed along an ice foliation in N₁N₁' while the detachment reached the underlying bedrock in M₁M₁'.**

Two parallel sections (Fig. 15B and Fig. 15C) were used to explain the different properties of the detachment surface. On the
475 east side, the collapse involved the entire glacial body down to the bedrock, which was exposed after the failure (Fig. 15C).
The basal till, that was located at the base of the glacieret, was completely washed out. On the west side, the collapse
occurred partly along a foliation plane and marginally at the bedrock interface (Fig. 15C). The presence of the basal till was
inferred from both RES images and direct observations of the residual ice surface on the western side of the post-failure
480 niche (Bondesan and Francese, 2023). This basal layer appears to thin towards the west, with a variable thickness, generally
estimated to be on the order of several decimetres.

Three different potential triggering factors, combined in several scenarios, were considered in the slope stability analysis
based on the Limit Equilibrium Method (Fig. 16): (1) the hydrostatic pressure in the crevasses filled with water, (2) the
hydraulic jacking pressure (Irvine-Fynn et al., 2011), and (3) the progressive reduction of friction along a weak layer at the
base of the ice body. This weak layer could be referred to as a mixture of melt water, till and ice (Huang et al., 2024).



485

Figure 16: Conceptualization of the model utilized for the numerical simulations. Driving forces: hydrostatic pressure in crevasses; hydraulic jacking pressure; reduction of the basal friction caused by the plasticization of a thin layer of subglacial ice (namely the weak layer) on top of the bedrock.

490

Table 1a. Base scenarios (A, B or C) considered for numerical simulations.

Scenario	Type	HYP in crevasse			HJP	WL	Factor of Safety (FoS)				
		c5a	c5b	c6			Computational method				
		(kN/m ²)			(kN/m ²)	(kPa)	Friction angle		Js	Jc	MCP/GLE
							(degrees)				
A	1	HYP	220						4.25	4.58	4.38
	2	HYP	220	220					2.97	3.23	2.87
	3	HYP	220	220	200				2.33	2.51	2.27
B		HJP			220				5.67	6.08	5.91
C	1	WL				208	21.6		5.84	6.23	5.86
	2	WL				156	19.2		5.16	5.50	5.40
	3	WL				104	16.8		4.42	4.70	5.27
	4	WL				52	14.4		3.97	4.22	4.86
	5	WL				10	13.0		3.56	3.75	3.66

A - HYP: hydrostatic pressure in crevasses (ck indicates crevasse id);
 B - HJP: hydraulic jacking pressure;
 C - WL: weak layer.

495



A first group of 9 numerical simulations (Table 1a) considered the separate contribution of each triggering factor (base scenarios), while a second group of 18 simulations (Table 1b) evaluated the combined effects of the various factors (combined scenarios). Three different computational methods were adopted for each simulation (see Supplementary Material for further details) resulting in 81 different slope stability models. In the base scenarios, the values of the Factor of Safety (FoS) were always greater than 1, corresponding to a stable condition, while in only three cases of the combined scenarios the FoS values were less than 1 (Table 1), evidencing the unstable condition.

Table 1b. Combined scenarios (AiB and AiBCj) considered for numerical simulations.

Scenario	Type	HYP in crevasse			HJP	WL	Factor of Safety (FoS)		Computational method			
		c5a	c5b	c6			Cohesion	Friction angle	Js	Jc	MCP/GLE	
		(kN/m ²)			(kN/m ²)	(kPa)	(degrees)					
AB	1	A1+B		220	220				3.25	3.49	3.25	
	2	A2+B		220	220	220			2.31	2.48	2.32	
	3	A3+B		220	220	200	220		1.79	1.92	1.75	
ABC	1	A1+B+C1		220	220	200	220	208	21.6	3.19	3.42	3.25
		A1+B+C2		220	220	200	220	156	19.2	2.79	2.98	2.84
		A1+B+C3		220	220	200	220	104	16.8	2.40	2.56	2.54
		A1+B+C4		220	220	200	220	52	14.4	2.35	2.50	2.37
		A1+B+C5		220	220	200	220	10	13.0	2.20	2.34	2.28
	2	A2+B+C1		220	220	200	220	208	21.6	2.24	2.41	2.27
		A2+B+C2		220	220	200	220	156	19.2	2.00	2.13	1.99
		A2+B+C3		220	220	200	220	104	16.8	1.62	1.72	1.69
		A2+B+C4		220	220	200	220	52	14.4	1.16	1.23	1.45
		A2+B+C5		220	220	200	220	10	13.0	0.71*	0.75*	1.19
	3	A3+B+C1		220	220	200	220	208	21.6	1.71	1.84	1.75
		A3+B+C2		220	220	200	220	156	19.2	1.54	1.65	1.55
		A3+B+C3		220	220	200	220	104	16.8	1.24	1.32	1.30
		A3+B+C4		220	220	200	220	52	14.4	0.83*	0.89*	0.93*
		A3+B+C5		220	220	200	220	10	13.0	0.42*	0.44*	0.71*

A - HYP: hydrostatic pressure in crevasses (ck indicates crevasse id);

B - HJP: hydraulic jacking pressure;

C - WL: weak layer;

* Factor of Safety (FoS) < 1.

5. Discussion

The failure of the Marmolada glacier is the result of an uneven combination of conditioning/predisposing and triggering factors in the quasi-extreme atmospheric conditions that occurred in the Alps during the late spring and summer of 2022. The overall evolution of the glacier itself, over the last century, has shown a marked retreat trend in terms of surface/area/volume (Fig. 4) and withdrawal rates (Fig. 3). This trend is fully comparable with what is generally observed for glaciers of the Alps



and worldwide world (Dyrgerov and Meier, 2004) as a consequence of ongoing global warming (Gilbert et al., 2010; Zemp
515 et al., 2015). Over the last 40 years, the withdrawal rate of the Marmolada glacier shows an accelerating trend with three
distinct time intervals (1985-2000; 2000-2020; post-2020) in which the slope of the average evolution curves (obtained by
local measurements) increases progressively (Fig. 3). Similar distinct time intervals could be observed also in the
area/surface area/volume graphs (Fig. 4). The retreat and disaggregation of the originally polythermal and largely warm-
based glacier in a permafrost environment caused the detachment and transformation of part of its former firm area into a
520 small, cold glacieret frozen to its permafrost bed at the detachment site with correspondingly critical thermohydraulic
conditions.

5.1 Predisposing factors at the detachment site

The longer-term conditioning/predisposing factors are mostly determined by the relationships between the geometry of the
glacieret and that of the carbonate bedrock. Further predisposing factors depend on the internal structure of the glacieret
525 itself, on the physics and stratigraphy of the basal layers, the permeability of the frozen sub- and peri-glacial glacial rocks,
and on the amount of snow precipitation.

The glacieret occupied a small bedrock niche in the generally steep slope (Fig. 12). It was partially suspended above a sub-
vertical wall and, since 2012, due to progressive melting, it was left without an ice foot which to some extent kept it
anchored to the underlying bedrock. In addition, warming-induced permafrost degradation (Gruber and Haeberli, 2007;
530 Rossi et al., 2022) is likely to have created critical instability conditions at the ice front.

Just below Rocca peak, the annual rate of lowering of the glacial surface was 0.58 m in the period 1990-2022 (Fig. 3C). At
the same time, increased extending flow towards the lost glacier connection caused a progressive opening of the crevasses,
which partly divided the ice body into blocks, favoring its instability, and creating additional storage for surface meltwater.
The underlying bedrock surface is steep, with an average slope of 33° below the crest, 39° across the failure edge, and 20° in
535 the middle and lower portions of the failure surface, respectively (Fig. 12B). The steep bedrock topography is often
recognized as a key predisposing factor for the initial sliding (Faillettaz et al., 2011), particularly when associated with
specific thermal conditions at the bedrock (Röthlisberger, 1981).

The winter 2021-2022 was characterized by a sum of new snow, from October to May, which was among the 10 lowest in
the last 100 years (Fig. 7B), as evidenced by the SAI anomaly index calculated on 8 stations in the Dolomites. Unfortunately,
540 there are no snow thickness sensors at the PRC station, but ~30 years of data (1991-2020) from the nearby RVL station
could be utilized as a reference and data from RVL (2615 m asl) and PZB (2905 m asl) stations, in the winter 2021-2022,
could be used for comparison instead of PRC. The snow cover in RVL highlights the early winter snowfall and the following
long period with little thickness of snow on the ground (about 0.5 m), which was increased by a precipitation in mid-
February. The snow cover increased again in late winter with the interposition of a melting period in the second tens of
545 April. This late-winter snow melted rapidly due to the mild temperature of the second decade of May onwards. In general,
fresh snow is highly reflective and therefore absorbs less solar radiation, but on the other hand it is much less compact and



therefore melts more quickly. In the Marmolada case the unpacked snow was prone to accelerated melting with high production of liquid water as compared to the typical compacted winter snow. In addition, due to the high porosity of the recent snow layer (Clifton et al., 2007), there is a very little surface runoff and melting water penetrate right into the glacier body as inferred by the satellite images taken two weeks before the failure. A rough estimate (Bondesan and Francese, 2023) indicates that around 15,000 m³ of melt water had infiltrated the glacier since mid-May. The snow cover in PZB has a similar trend to RVL despite this station (facing the Marmolada glacier) is located ~300 m higher in elevation than RVL.

The limited snow cover in the months of February and March could be observed in the images taken by the webcam positioned at Cima Padon, right in front of the Marmolada glacier, and available online (https://portavescovo.panomax.com/). The failure site appears to be covered by snow in the images taken in April and May. The temperature in February was relatively mild, while in March it was much colder. This particular temperature trend could be the cause of a different thermal inertia in the exposed glacial body.

Evolution of permafrost conditions around the failure zone is crucial to get better insight in possible collapse mechanisms. A strong contrast exists between the sun-exposed, ice-free south wall of Marmolada with its warm, probably unfrozen rocks, and the cold northern slope facing away from the sun and with widespread permafrost (Boeckli et al., 2012). Where bedrock of the northern slope has remained free of glaciers during past decades, its temperature can be estimated at a few °C below freezing temperature, probably close to 0°C at lower altitudes, around 2400-2600 m asl, and reaching -1°C to -4°C towards the uppermost parts. These temperature estimates were confirmed by several shots taken with a drone-mounted thermal imaging camera the morning after the failure on the newly exposed bedrock. With such estimated surface temperatures, permafrost depth may in places exceed several tens of m (Etzelmüller et al., 2020; Rossi et al., 2022). Ice temperatures recorded several tens of cm within the walls of some WWI tunnels, dug in the Marmolada glacier in 1917 (Hess, 1940), in the elevation range 2800-3200 m asl, showed average values of -1.32°C in tunnel “32” (located in the vicinity of the failure site) and of -1.27°C in tunnel “S” (located ~700 m west of the failure site). With moderately cold conditions such as on the northern side of the Marmolada, glaciers tend to be polythermal or at least partially warm-based (Wilson and Flowers, 2013) as also inferred computing RES velocity data for this glacier (Forte et al., 2020). In the Alps, pervious firn zones, warmed up by percolating and refreezing meltwater, are temperate up to altitudes between approximately 3500 and 3900 m above sea level (Haeberli and Alean 1985; Suter et al., 2001; Bohleber, 2019) while the impermeable ice of the ablation zones may be cold.

The LIA glacier at the Marmolada site (Fig. 8A) was predominantly temperate/warm-based and only its very top portions and its lowest margins may have been cold and partially frozen to bedrock indicating that bedrock underneath the LIA glacier was largely unfrozen.

As mentioned, the stability in the detachment zone was recently lowered by the disconnection of the failed ice body from the former glacier by the opening of large transversal crevasses but it was also strengthened by the transformation from a warm-based firn area with basal sliding to a cold ice body with permafrost penetration into the bedrock underneath the ice.



580 Permafrost penetration may still be in its initial stage but is likely to already have reduced the hydraulic permeability of the karstic dolomitic rocks underneath the ice through the process of ground freezing. This permeability reduction could have helped building up high water pressures in the ice body.

The vertically curved geometry of the median crevasse, clearly visible after the failure, suggests that the glacier was mostly deformed under the action of the gravity force with negligible basal sliding, hence further confirming the hypothesis of a
585 local cold ice base.

5.2 Triggering factors

A small earthquake had originally been considered the factor causing the initial sliding of critical glacieret block thus triggering the entire failure. Such occurrences are quite frequent (Podolskiy et al., 2010) and the hypothesis was likely suggested by analogy to events associated with the recent Gorkha earthquake (Pettenati et al., 2023) that affected the
590 Kathmandu valley in the Himalaya region in April 2015, causing the Langtang Valley disaster (Fujita et al., 2017). The same earthquake also triggered an ice avalanche (Kargel et al., 2016) that struck Everest base camp killing 24 people and injuring 61 causing the deadliest disaster on the mountain ever. However, on July 3, 2022, the NOAN seismic network reports only three events which are far away from the Marmolada glacier (Table 2). Two events occurred several hours before while the third event occurred approximately two hours later. No suspicious seismic activity was recorded nearby the Marmolada
595 glacier the day of the collapse.

Table 2. Seismic events occurred on July 3, 2022 in northern Italy and surrounding regions.

Site	Region	Magnitude	CEST	Latitude	Longitude
		M_L	hh:mm:ss	decimal degrees N	decimal degrees E
Forni di Sotto (F. Venezia-Giulia)	Eastern Alps	1.0	6:33:40	46.336	12.621
Giogo dello Stelvio (Alto-Adige)	Central Alps	0.5	7:18:44	46.558	10.482
Sassuolo (Emilia-Romagna)	N. Apennines	2.3	17:53:25	44.545	10.798

The seismological localization of the Marmolada collapse and avalanche is accurate as it corresponds to the real position
600 within a reasonable error range, despite there being no seismic stations in the north-east quadrant. The waveform is typical of an avalanche or of an ice-rock fall (Fig. 14B).

The matching filter method (Gibbons and Ringdal, 2006; Sukan et al., 2014) was applied on the time series of the AGOR station to dispel further doubts that the collapse was triggered by an earthquake. The collapse-related time series considered the two minutes of the event itself and the three preceding minutes. Two low-magnitude seismic shocks occurred in 2023
605 (M0.9 on April 19th at 22:12:50 and M1.3 on July 10th at 22:47:41) were used as the template for the cross-correlation. The matching process resulted in a degree of cross-correlation that did not exceed the value of 0.40, confirming that the failure was not triggered by a seismic shock.



610 Neglecting the seismic shock, the overall triggering factor should be sought in a complex interaction between the extremely high air temperatures, which lasted for more than two months, and the resulting thermo-hydraulic conditions of the ice of the glacieret and of the bedrock.

There is no doubt about the temperature anomaly that characterized the late spring and early summer of 2022. At PRC station the 70 days preceding the collapse showed monthly temperatures (max, avg and min) not only above the standard deviation range for the 30-year period 1990-2020 but these values turned out to be absolute maxima (Fig. 6A1).

615 The effect of the elevate temperatures is two-fold: it represented an intense heatwave over the glacier (Chen et al., 2023) and the exposed bedrock. This enhanced the production of meltwater, which penetrated into the crevasses of the glacieret, filling them and warming the ice down to their bottom. The latter phenomenon may have been amplified by the asymmetry between the warm south face and the cold northern slope of the mountaion. The strong north-south thermal contrast in the mountain ridge induces a marked horizontal heat flow (Noetzli et al., 2007), affecting the failure zone that is located just below the crest (Fig. 2). The marked warming up of the uppermost rock layers is clearly evidenced by the temperature data from the
620 PZB borehole (Fig. 7A). On July 3, 2022, the positive thermal anomaly reaches down to 3.5 meters below the surface and it represents an absolute maximum in the ten years of observation.

A detailed analysis of the failure surface provides further information on the thermal conditions of the coupled bedrock-ice system at the time of the failure. The failure occurred along a rather complex surface. Considering the frontal wedge, it is clear that at least two thirds of the failure plane developed along an envelope surface of foliation planes (Fig. 9B). In its
625 southern, central, and western part it is mostly a detachment within the ice and not a newly formed failure surface, while in the eastern portion the bedrock is exposed. To the south, a thick ice layer was left on top of bedrock after the failure (area marked a0 in Fig. 9B) while to the north the residual ice layer is very thin (area marked s0 in Fig. 9B) but it took several days before it melted completely, as documented in several videos taken in the weeks after the failure. Similarly to the failure of the Altel glacier in 1895 (Faillettaz et al., 2011) a large portion of basal ice is clearly frozen to bedrock at the
630 north-west front (Fig. 9B). Many foliations are visible in the glacial body (Fig. 9A) and they represent ductile structures that could play a major role in both water-routing (Jennings and Hambrey, 2021) and the development of a failure mechanism. Foliations, which could result from migration of air bubbles and fine debris (Hooke and Hudleston, 1978), are best depicted on the sub-vertical ice face of the fracture scarp, where they show spatial extents of several decimeters (see Supplementary Material). In the RES signature (Fig. 11A) there is with no evidence of warm ice (sensu Forte et al., 2020). The residual
635 portion of the glacieret seems to be then comprised of moderately cold ice, in agreement with the prediction curve (Haeberli et al., 2004a; Fig. 8B). The high englacial reflectivity of the foliation planes indicates the presence of a significant contrast in electrical impedance and therefore the presence of major sub-horizontal discontinuities in the ice body that affected the development of the failure plane during rupture. The thin basal layers interposed between the ice and the underlying bedrock, affect the overall stability of the glacieret. Unfortunately there is very little evidence about the existence and spatial
640 distribution of this basal layer along the failure surface, with the exception of some deposits visible on the residual front of the glacieret (marked tbt in Fig. 9B).



Regarding the presence of flowing melt water at the base of the glacier, some observations could be made. There is no evidence of a frontal discharge in the aerial image (SAT, 2022) and in the satellite images (Fig. 9A, Fig. 10A) taken the day before and a few days before the collapse respectively. This indicates that the meltwater is not routed in a channelized subglacial drainage, as it is common for larger warm-based glaciers (Röthlisberger and Lang, 1987; Richards et al., 1996). On the contrary, there is clear evidence of water outflowing from the eastern edge of the median crevasse routed along a bédrière (Fig. 9A), confirming that an englacial drainage network is not developed. Anyhow, englacial water is present in the glacieret but its cold ice frozen to permafrost rocks prevents basal or subglacial water flow (Paterson, 1994). Insights into the significance of the driving forces can also be obtained from numerical simulations of glacier slope stability. The overall failure mechanism can be reasonably interpreted as a simple frictional model of a solid mass sliding along a surface, and for this reason the LEM was used. The 2D approach used for the simulation has certainly some limitation but the currently available parameters prevent a meaningful 3D approach. In addition, it is worth mentioning that the failed ice body, to the west, was firmly joined to the western glacial shoulder which did not collapse. This limit results in an underestimation of the FoS values calculated via a simple 2D approach.

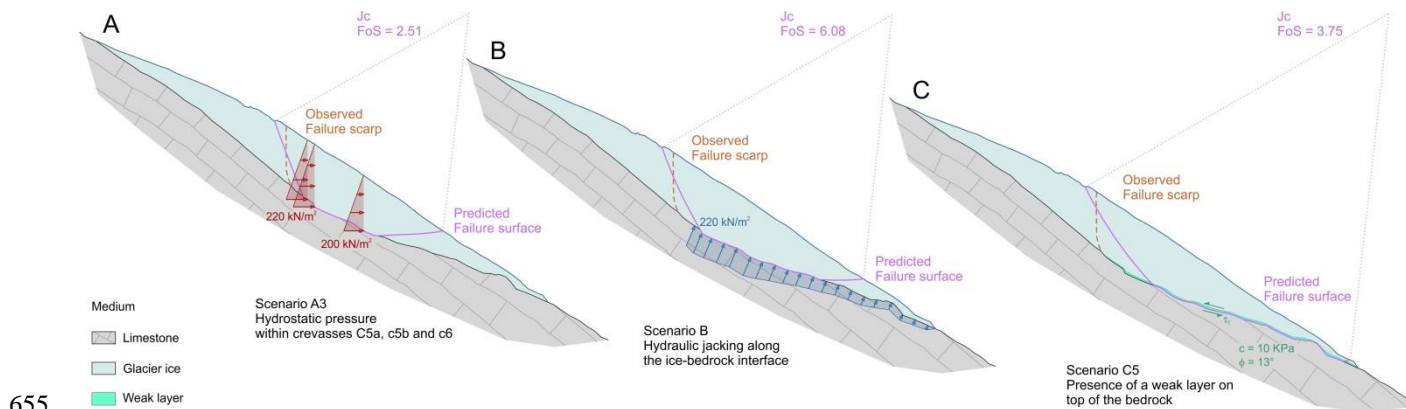


Figure 17: Numerical simulations: base scenarios. (A) Scenario A3 - hydrostatic pressure acting on crevasses 5a, 5b and 6; (B) Scenario B - hydraulic jacking pressure acting along the ice-bedrock interface; (C) Scenario C - reduction of the basal friction caused by a weak layer on top of the bedrock in the worst case ($c=10$ kPa; $\phi=13^\circ$). See text and Table 1a for details.

The base scenario, conceptualized in Fig. 16, weights the effects of three single causes of instability: hydrostatic pressure in crevasses, hydraulic jacking pressure, and presence of a weak layer at the base. The nature of this weak layer essentially depends on its genesis and, excluding the presence of a basal drainage network as indicated by the absence of a frontal water discharge, various hypotheses can be made on the causes that determined its formation: (1) Transfer of heating from the outcropping rocks forming the east shoulder of the niche could have caused the softening/plasticization of the ice at the ice-bedrock interface resulting in a plastic mixture of water, ice and debris (Huang et al., 2024). This could be particularly true in consideration of the extreme thermal conditions, which occurred during the late spring and early summer of 2022 and must have affected the fragile equilibrium of the permafrost. (2) The large volume of meltwater stored in the crevasses,



because of the absence of a continuous drainage network, caused an overpressure (Church et al., 2021) that finally resulted in the water forcing its way throughout the basal till layer or a foliation surface, thus forming a locally connected drainage system (Kavanaugh and Clarke, 2001). In both cases, the shear stress could have easily exceeded the resisting forces causing instability. Moreover, warm permafrost with temperatures between about 0°C and -1.5°C contains ice with unfrozen water. Such “warm permafrost” is weaker not only than colder but also than unfrozen bedrock (Davies et al., 2001; cf. Fig. 8C). The resistance of basal rocks may also have become critical (Fig. 15B); this is a further element suggesting including the weak layer in the model.

In the three base scenarios (Table 1a and Fig. 17) the minimum FoS is largely above the value of 1 for the three different computational methods. The values of FoS computed with the different methods are more or less comparable. The “Janbu corrected” (Jc) will therefore be considered for the purpose of this discussion.

The summed effects of the hydrostatic pressure in multiple crevasses lower the FoS to a minimum value of 2.51 (Fig. 17A) while the effect of the hydraulic jacking pressure alone seems to be negligible, as the FoS value is significantly higher than the previous scenarios indicating overall stability (Fig. 17B). The weak layer alone does not generate instability also when modeled using the minimal values for the c - ϕ (cohesion - friction angle) pairs (Fig. 17C) as it results in a FoS of 3.75. The predicted failure surface is surprisingly close to reality in the case of hydraulic jacking pressure alone (Fig. 17C and Fig. 7B), albeit along a cross section shifted less than 10 m westward compared to the cross-section modelled in the simulations.

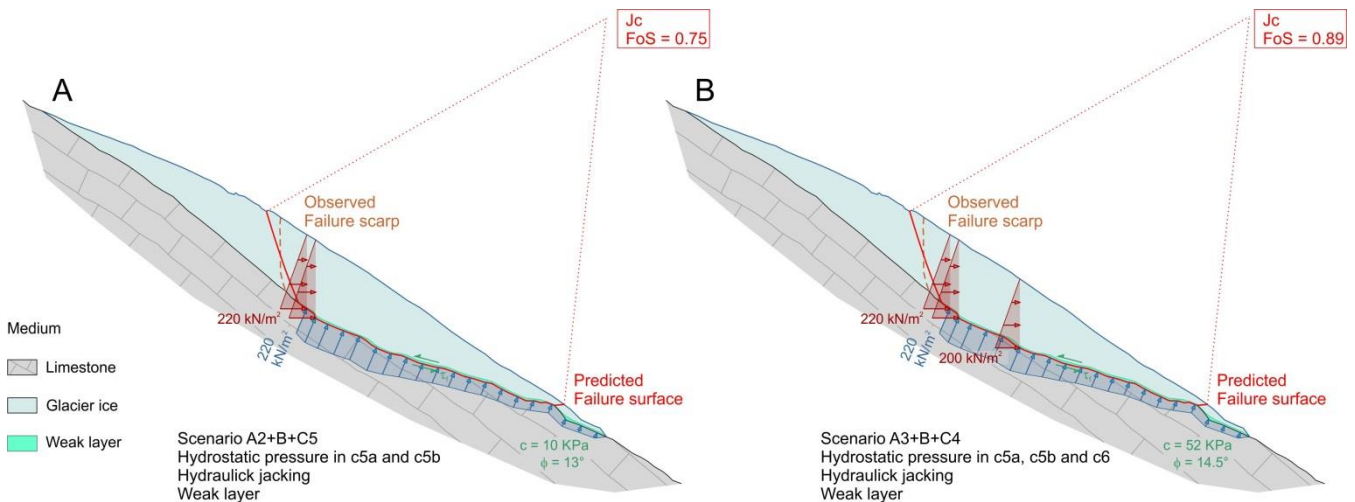


Figure 18: Numerical simulations: combined scenarios. (A) The instability condition, with relative FoS less than 1, is reached in the scenario A2 (hydrostatic pressure in two crevasses) + B (hydraulic jacking pressure) + C5 (worst c , ϕ pair in the weak layer); (B) The instability condition, with relative FoS less than 1, is reached in the scenario A3 (hydrostatic pressure in all crevasses) + B (hydraulic jacking pressure) + C4 (second worst c , ϕ pair in the weak layer). See text and Table 1b for details..

The minimum FoS (2.51) in the three basic scenarios corresponds to the hydrostatic pressure condition acting in all crevasses. Therefore, it seems possible to exclude the single driving action for the triggering of the collapse and this finding



is consistent with what happened in other similar cases (Mortara and Dutto, 1990; Haeberli et al., 2004b; Faillettaz et al., 2015). The FoS was always largely greater than 1 in the 27 simulations in the group of the base scenarios.

The combined scenarios weight the effect of different associations of the factors of instability. The FoS is always greater than 1 in case of hydrostatic pressure associated with hydraulic jacking pressure (scenarios A_i+B in Table 1b) with a minimum of 1.92, suggesting that the driving action of meltwater alone cannot induce the failure. The inclusion of the weak layer determines conditions of instability (in combination at least with scenario A2, which considers the hydrostatic pressure in two of the three crevasses) but only in the condition of minimum resistance (scenario C5) of the weak layer itself (Fig. 18A). The FoS in the A_2+B+C_5 scenario drops to 0.75. The predicted failure surface almost reaches the front of the glacieret. This result is consistent with the model used for the simulations, in which the weak layer was extended down to the front of the glacieret. This predicted failure surface corresponds to reality for the ice volume located in the eastern half of the glacieret (Fig. 18B). Considering finally the hydrostatic pressure acting on all three crevasses (scenario A_3+B+C_j in Table 1b), instability already occurs starting from a weak layer characterized by a couple of parameters $c-\phi$ (C4) which is the second most unfavourable among those modelled (Fig. 18B). The FoS in the A_2+B+C_5 scenario drops to 0.89. The FoS was less than 1 in just 8 of the 54 simulations in the group of the combined scenarios.

The considered triggering causes are almost equivalent as none alone prevails over the others. However, it could be possible to establish a “ranking”, considering the values of FoS, based on how close they are to one, although they are greater than one. In this sense, the worst triggering factor relates to the water-filled crevasses (FoS = 2.51, lower than the others). It is followed by the weak layer characterized by the worst parameters (FoS = 3.75). The least important is hydraulic jacking (FoS = 6.08). However, there are many uncertainties about the parameters of the weak layer.

As far as the predisposing factors are concerned, the formation of deep crevasses in cold ice frozen to permafrost rocks appears to represent the most critical predisposing condition. Without their presence, hydraulic jacking would be more difficult to initiate and, as a chain, the degradation of the weak layer would also be slower. Moreover, the loss of shear strength of the basal interface is connected with the decrease in effective stresses due to the increase in water pressure. In other words, it can be assumed that the other predisposing/triggering factors also depend upon the development of the crevasses.

The “sine qua non” condition for the instability of the ice mass that collapsed on 3 July 2022 is then a combined action of three instability factors, none of which alone determines a FoS condition lower than 1.

Finally, some considerations must be made on the predictability of the glacial collapses. It is known that cold-based glaciers show very few precursors detectable at the surface (Röthlisberger, 1981), while in case of warm-based glaciers some surface effects could be observed in the imminence of the break-off (Faillettaz et al., 2011). Surface velocity is the parameter to be monitored but, in general, the time window for predicting a failure is very short and no longer than a few days or at best weeks (Pralong et al., 2005), with the danger of false alarms. Quantitative glacier monitoring is probably more effective than visual glacier observations but it is also more costly and then possibility of false alarms must be taken into account. Glacier seismicity (Walter et al., 2009) could be used to correlate ice quakes with ice dynamics but this seismicity is also controlled



by surface melting and changes in subglacial water pressure (Mikesell et al., 2012), resulting in inherent difficulty in transposing ice quake occurrences into an effective collapse precursor.

730 An alternative strategy may be to create hazard scenarios based on sets of key parameters (e.g. temperature, snow cover, melting rate, etc.) to be cost-effectively collected or reliably estimated but only after having achieved a full knowledge on glacier (including major crevasses) and bedrock morphology. A good control on the glacier geometry allows for the use of advanced ice flow models (Zekollari et al., 2022) that could be turned into effective numerical simulations of stability. Current technology allows the simple and cost-effective acquisition of time-lapse geophysical images of almost all Alpine glaciers (Ruols et al., 2023) via UAV-mounted broadband RES antennas, which could be flown just above the glacier surface, preventing the loss of resolution that generally affects helicopter-based RES surveys.

735 5. Conclusions

A thorough compilation of information on recent morpho-climatic evolution combined with in situ geophysical imaging, seismological analysis and geothermal data was used as a basis for numerical back-analysis concerning the deadly 2022 ice collapse at the Marmolada Glacier.

740 The detachment zone was originally part of the the probably temperate firn/accumulation zone of the Little Ice Age glacier. As a consequence of the warming-induced disaggregation of the LIA glacier, it became y – during at least the last three decades – an isolated cold glacieret consisting of massive, impermeable but crevassed ice. Its ice temperature can be estimated at some -2°C , i.e., relatively close to melting conditions but with at least partially freezing or frozen bed. In proximity of the crest, continued climate-induced warming of the nearby south face and onset of cooling related to changing ice conditions on the northern slope, increased the thermal contrast and related sub-horizontal heat flow across the mountain.

745 The collapse was caused by an uneven combination of predisposing and triggering factors which, acting in different time frames and with variable weights, favoured instability until the tragic failure occurred in July 2022.

The progressive retreat of the glacier, its fragmentation into smaller individual ice bodies, together with the high slope inclination and the asymmetric permafrost conditions close to the ridge with a warm south face certainly influenced the conditioning/predisposition of the collapse. Further conditioning elements must have been the complicated thermal settings of the ice-bedrock interface, the presence of low-angle discontinuities such as foliations in the ice and/or the discontinuous layers of basal till deposits.

750 The probably most influential triggering factors are associated with minimal winter snowfall and the prolonged thermal anomaly that characterized late spring and early summer 2022, considered as a sort of an “annus horribilis”. The marginal thickness of low-permeable snow layers and especially the extreme air temperatures resulted in an excess of meltwater penetrating deep into the glacier. In fact, water filling the deep crevasses could have produced subglacial water pressures in excess of floating conditions. Its freezing due to the cold crevasse walls induced not only efficient warming by latent heat



exchange but also added downslope stress. The absence of a drainage network created the condition for the development of an increasing hydraulic over-pressure.

760 An earthquake as the final triggering mechanism could be excluded and results from numerical simulations suggested that triggering of the final collapse must most probably be seen as a simultaneous interaction of hydrostatic pressure, hydraulic jacking pressure, and reduction of the basal friction caused relating to a weak basal layer. The weak basal layer appears to be a key factor of the failure. Its evolution may be associated with permafrost degradation at the ice-bedrock interface, which resulted in a local plasticization of basal ice and fine glacial deposits.

765 Numerical back-analysis was conducted with the LEM creating bi-dimensional base and combined scenarios of driving forces but it should be noted that some resisting forces, due to the real three-dimensional shape (i.e. lateral failure), were neglected, partly limiting the effectiveness of numerical simulations. The 3D morphology of the niche and the existence of mild counter slopes in the calcareous bedrock are further aspects that could not be fully considered in a simple 2D modeling approach. Ranking of the predisposing/triggering factors accurately is not a straightforward task, but it's possible that the most influential predisposing factor is related to the progressive widening of crevasses while the crucial triggering factor
770 could be associated with the water infill of crevasses.

Future improvement of the numerical simulations will include a full 3D modelling of the failure, based on new borehole measurements of the ice and bedrock temperatures and high-resolution RES geophysical images data that are planned to be collected.

775 Determinist modeling of glacier instability seems to be really complicated and feasible only in specific conditions and its effectiveness depends upon the control on the different variables. Extensive monitoring is likewise costly and hardly implementable in a systematic manner. The generation of instability scenarios could be a reasonable compromise if based on the standard parameters collected with the meteorological network associated with time-lapse geophysical imaging of the glacier geometry and physics.

CRedit authorship contribution statement

780 RF and AB both designed the study, organized, and participated in geophysical field surveys along with SP and MG. RF re-organized, and re-structured the various data types implementing the GIS and the database. GR processed the satellite images. WH and MV provided information on climatic variables and permafrost. FP and DR processed the seismological data. RV implemented the numerical models and conducted the simulations. All the authors equally contributed to the analysis of the results and to the writing of the manuscript.



785 Declaration of competing interest

The authors declare that they have no known competing financial interests or personal relationships that could have appeared to influence the work reported in this paper.

Funding

790 Research was funded by: FFABR 2017 (MIUR, Francese); FIL 2019 (University of Parma, Francese); DOR (Dotazione Ordinaria Ricerca) 2015–2021 (University of Padova, Bondesan); PRAT2013 (Progetto di Ateneo 2013, University of Padova, Bondesan). Other funds were provided by the National Institute of Oceanography and Applied Geophysics (OGS).

Data availability

Some of the data could be made available upon request while some others are confidential.

Acknowledgments

795 The authors gratefully thank Nicola Casagli (UNIFI) for providing and processing TLS data collected just after the collapse. The authors are also grateful to Riccardo Percacci for his help and suggestions in applying the matched-filter method. Particular thanks to Nuccio Bucceri of Land & Technology Srl for his aid in processing the IR images. Special thanks to Provincia di Trento and to the cartographic bureau of Regione del Veneto for providing past satellite/aerial imagery and LIDAR data and to Alberto Carton for providing historical maps. AB is a research fellow at the University of Stellenbosch,
800 and RF is a research fellow at the National Institute of Oceanography and Applied Geophysics.

References

- Aggarwal, A., Jain, S. K., Lohani, A. K., and Jain, N.: Glacial lake outburst flood risk assessment using combined approaches of remote sensing, GIS and dam break modelling, *Geomatics Nat. Hazards Risk*, 7(1), 18–36, doi:10.1080/19475705.2016.1144652, 2016.
- 805 Alean, J.: Avalanches de glace, *Alpen*, 61, 3, 121-132, 1985.
- Allen, S., Frey, H., Haeberli, W., Huggel, C., Chiarle, M., and Geertsema, M.: Assessment principles for glacier and permafrost hazards in mountain regions, *Oxford Res. Encyc. Nat. Haz. Sci.*, doi:10.1093/acrefore/9780199389407.013.356, 2022.



- Antonelli, R., Barbieri, G., Dal Piaz, G. V., Dal Pra, A., De Zanche, V., Grandesso, P., Mietto, P., Sedeà, R., and Zanferrari,
810 A.: Carta geologica del Veneto 1: 250.000 - Una storia di cinquecento milioni di anni, Geological Map of the Veneto Region
1:250,000, 32 pp., 1990.
- Bessette-Kirton, E. K., and Coe, J. A.: A 36-Year Record of Rock Avalanches in the Saint Elias Mountains of Alaska, With
Implications for Future Hazards, *Front. Earth Sci.*, 8, 293, doi:10.3389/feart.2020.00293, 2020.
- Bieniawski, Z. T.: Engineering rock mass classifications, John Wiley & Sons, New York, 251 pp., ISBN-13:
815 9780471601720, 1989.
- Biskaborn, B.K. and 47 co-authors.: Permafrost is warming at a global scale. *Nature Communications*, 10, 264, Doi:
10.1038/s41467-018-08240-4, 2019.
- Bodin, X., Krysiński, J. M., Schoeneich, P., Le Roux, O., Lorier, L., Echelard, T., et al.: The 2006 collapse of the Bérard
rock glacier (Southern French Alps), *Permafr. Periglac. Process.*, 209-223, doi:10.1002/ppp.1887, 2017.
- 820 Boeckli, L., Brenning, A., Gruber, S., and Noetzli, J.: Permafrost distribution in the European Alps: calculation and
evaluation of an index map and summary statistics, *Cryosphere*, 6, 807–820, doi:10.5194/tc-6-807-2012, 2012.
- Bohleber, P.: Alpine Ice Cores as Climate and Environmental Archives, *The Oxford Encyclopedia of Climate Science*,
doi:10.1093/acrefore/9780190228620.013.743, 2019.
- Bolch, T., Kulkarni, A., Kääb, A., Huggel, C., Paul, F., Cogley, J. G., Frey, H., Kargel, J. S., Fujita, K., Scheel, M.,
825 Bajracharya, S., and Stoffel, M.: The state and fate of Himalayan glaciers, *Science* 336.6079, 310-314,
doi:10.1126/science.1215828, 2012.
- Bondesan, A., and Francese, R. G.: The climate-driven disaster of the Marmolada Glacier (Italy), *Geomorphology*, 431,
108687, doi:10.1016/j.geomorph.2023.108687, 2023.
- Bondesan, A., Carton, A., and Laterza, V.: Leo Handl and the ice city (Marmolada Glacier, Italy), *Rendiconti Online della*
830 *Società Geologica Italiana*, 36, 31–34, doi:10.3301/ROL.2015.137, 2015.
- Bosellini, A.: *Geologia delle Dolomiti*, Athesia, ISBN-13: 9788870148893, 1996.
- Carton, A., Bondesan, A., and Benetton, S.: Marmolada, la regina delle Dolomiti, *Itinerari Glaciologici sulle Montagne*
Italiane 3, Itinerari 19A e 19B, Comitato Glaciologico Italiano, 89–212 pp., 2017.
- Chen, W., Yao, T., Zhang, G., Woolway, R. I., Yang, W., Xu, F., and Zhou, T.: Glacier surface heatwaves over the Tibetan
835 Plateau, *Geophysical Research Letters*, 50, e2022GL101115, doi:10.1029/2022GL101115, 2023.
- Chiarle, M., Geertsema, M., Mortara, G., Clague, J. J.: Relations between climate change and mass movement: perspectives
from the Canadian Cordillera and the European Alps, *Glob. Planet. Chang.*, 202, 103499,
doi:10.1016/j.gloplacha.2021.103499, 2021.
- Chiarle, M., Viani, C., Mortara, G., Deline, P., Tamburini, A., and Nigrelli, G.: Large glacier failures in the Italian Alps over
840 the last 90 years, *Geogr. Fis. Dinam. Quat.*, 19-40, doi:10.4461/GFDQ.2022.45.2, 2022.
- Church, G., Bauder, A., Grab, M., and Maurer, H.: Ground-penetrating radar imaging reveals glacier's drainage network in
3D, *Cryosphere*, 15, 8, 3957–3988, doi:10.5194/tc-15-3975-2021, 2021.



- Clifton, A., Manes, C., Rüedi, J-D., Guala, M., and Lehning, M.: On Shear-Driven Ventilation of Snow, *Boundary-Layer Meteorology*, 126, 249–261, doi:10.1007/s10546-007-9235-0, 2007.
- 845 CGI - Comitato Glaciologico Italiano, CNR - Consiglio Nazionale delle Ricerche: *Catasto dei Ghiacciai Italiani, Anno Geofisico Internazionale 1957-1958 - Ghiacciai delle Tre Venezie e dell'Appennino*, Comitato Glaciologico Italiano, Torino, 4, 309 pp, 1962.
- Crepaz, A., Baldo, M., Frigerio, S., Gabrieli, J., Galuppo, A., Magnabosco, L., Mantovani, M., and Pasuto, A.: *Permafrost in Veneto Region: distribution, analysis and potential environmental effects*, PERMANET Project-Alpine Space Programme, Regione del Veneto, Technical Report, 100 pp., 2011.
- 850 Crepaz, A., Cagnati, A., and De Luca, G.: *The evolution of Dolomitic glacier during the last century*, *Mountains Under Watch*, Forte di Bard, Aosta, February, 20-21, 2013.
- CRS – Centro Ricerche Sismologiche, National Institute of Oceanography and of Applied Geophysics – OGS, *Real Time Seismic Network*, <https://rts.crs.inogs>, 2024.
- 855 D'Alessandro, A., Luzio, D., D'Anna, G., and Mangano, G.: *Seismic Network evaluation through simulation: an application to the Italian national Seismic Network*, *Bull. Seismol. Soc. Am.*, 101, 3, 1213–1232, doi:10.1785/0120100066, 2011.
- Davies, M. C. R., Hamza, O., and Harris, C.: *The effect of rise in mean annual temperature on the stability of rock slopes containing ice-filled discontinuities*, *Permafr. Periglac. Process.*, 12, 69–77, doi:10.1002/ppp.376, 2001.
- Dutto, F., Godone, F., and Mortara, G.: *L'écroulement du glacier supérieur de Coolidge (Paroi nord du Mont Viso, Alpes occidentales)*, *Rev. Géogr. Alp.*, 79(2), 7-18, doi:10.3406/rga.1991.3597, 1991.
- 860 Dyurgerov, M. B., and Meier, M. F.: *Glaciers and the Changing Earth System: A 2004 Snapshot*, 58 pp., *Inst. Arct. Alp. Res.*, Univ. Colorado, 2004.
- Egli, P., Irving, J., and Lane, S.: *Characterization of subglacial marginal channels using 3-D analysis of high-density ground-penetrating radar data*, *J. Glaciol.*, 67, 759–772, doi:10.1017/jog.2021.26, 2021.
- 865 Etzelmüller, B., Guglielmin, M., Hauck, C., Hilbich, C., Hoelzle, M., Isaksen, K., Noetzli, J., Oliva, M., and Ramos, M.: *Twenty years of European mountain permafrost dynamics – the PACE legacy*, *Environ. Res. Lett.*, 15, 104070, doi:10.1088/1748-9326/abae9d, 2020.
- Faillettaz, J., Funk, M., and Vincent, C.: *Avalanching glacier instabilities: review on processes and early warning perspectives*, *Rev. Geophys.*, 53, 203–224, doi:10.1002/2014RG000466, 2015.
- 870 Faillettaz, J., Sornette, D., and Funk, M.: *Numerical modeling of a gravity-driven instability of a cold hanging glacier: reanalysis of the 1895 break-off of Altelsgletscher, Switzerland*, *J. Glaciol.*, 57, 205, 817–831, doi:10.3189/002214311798043852, 2011.
- Falaschi, D., Kääh, A., Paul, F., Tadono, T., Rivera, J. A., and Lenzano, L. E.: *Collapse of 4Mm³ of ice from a cirque glacier in the Central Andes of Argentina*, *Cryosphere*, 13, 997–1004, doi:10.5194/tc-13-997-2019, 2019.
- 875 Fischer, A., Stocker-Waldhuber, M., Frey, M., and Bohleber, P.: *Contemporary mass balance on a cold Eastern Alpine ice cap as a potential link to the Holocene climate*, *Sci. Rep.*, 12, 1331, doi:10.1038/s41598-021-04699-2, 2022.



- Forte, E., Santin, I., Colucci, R., Dossi, M., Guglielmin, M., Pipan, M., Roncoroni, G., and Žebre, M.: GPR data analysis for cold and warm ice detection and characterization in polythermal glaciers, 18th Int. Conf. Ground Penetrating Radar, Golden, Colorado, USA, 14–19 June, Soc. Explor. Geophysicists, 69–72, 2020.
- 880 Francese, R. G., Bondesan, A., Giorgi, M., Picotti, S., Carcione, J., Salvatore, M. C., Nicolis, F., and Baroni, C.: Geophysical signature of a World War I tunnel-like anomaly in the Forni Glacier (Punta Linke, Italian Alps), *J. Glaciol.*, 65, 253, 798–812, doi:10.1017/jog.2019.59, 2019.
- Fretwell, P., Pritchard, H. D., Vaughan, D. G., Bamber, J.L., Barrand, N. E., et al.: Bedmap2: improved ice bed, surface and thickness datasets for Antarctica, *Cryosphere*, 7, 375–393, doi:10.5194/tc-7-375-2013, 2013.
- 885 Fujita, K., Inoue, H., Izumi, T., Yamaguchi, S., Sadakane, A., Sunako, S., Nishimura, K., Immerzeel, W. W., Shea, J.M., Kayastha, R. B., and Sawagaki, T.: Anomalous winter-snow-amplified earthquake-induced disaster of the 2015 Langtang avalanche in Nepal, *Nat. Hazards Earth Syst. Sci.*, 17, 5, 749–764, doi:10.5194/nhess-17-749-2017, 2017.
- Gascoïn, S., and Berthier, E.: Remote sensing analysis of Marmolada (Italy) and Juuku pass (Kyrgyzstan) glacier collapses, EGU General Assembly 2023, Vienna, Austria, 24–28, EGU23-14011, doi:10.5194/egusphere-egu23-14011, 2023.
- 890 Gentili, S., Sugan, M., Peruzza, L., and Schorlemmer, D.: Probabilistic completeness assessment of the past 30 years of seismic monitoring in north-eastern Italy, *Phys. Earth Planet. Inter.*, 186, 81–96, doi:10.1016/j.pepi.2011.03.005, 2011.
- Gibbons, S. J., and Ringdal, F.: The detection of low magnitude seismic events using array-based waveform correlation, *Geophys. J. Int.*, 165, 1, 149–166, 2006.
- Gilbert, A., Vincent, C., Gagliardini, O., Krug, J., and Berthier, E.: Assessment of thermal change in cold avalanching
895 glaciers in relation to climate warming, *Geophys. Res. Lett.*, 42, 6382–6390, doi:10.1002/2015GL064838, 2015.
- Gilbert, A., Wagnon, P., Vincent, C., Ginot, P., and Funk, M.: Atmospheric warming at a high elevation tropical site revealed by englacial temperatures at Illimani, Bolivia (6340 m above sea level, 16°S, 67°W), *J. Geophys. Res.*, 115, D10109, doi:10.1029/2009JD01296, 2010.
- Greene, C. A., Gardner, A. S., Wood, M., and Cuzzone, J. K.: Ubiquitous acceleration in Greenland Ice Sheet calving from
900 1985 to 2022, *Nature*, doi:10.1038/s41586-023-06863-2, 2024.
- Gruber, S., and Haeberli, W.: Permafrost in steep bedrock slopes and its temperature-related destabilization following climate change, *J. Geophys. Res.*, 112, F02S18, doi:10.1029/2006JF000547, 2007.
- Gruber, S.: Derivation and analysis of a high-resolution estimate of global permafrost zonation, *Cryosphere*, 6, 221–233, doi:10.5194/tc-6-221-2012, 2012.
- 905 Haeberli, W., and Alean, J.: Temperature and accumulation of high-altitude firn in the Alps, *Ann. Glaciol.*, 6, 161–163, 1985.
- Haeberli, W., and Hoelzle, M.: Application of inventory data for estimating characteristics of and regional climate-change effects on mountain glaciers: a pilot study with the European Alps, *Ann. Glaciol.*, 21, 206–212, 1995.
- Haeberli, W., Frauenfelder R., Kääb, A., and Wagner, S.: Characteristics and potential climatic significance of “miniature ice
910 caps” (crest- and cornice-type low-altitude ice archives), *J. Glaciol.*, 50, 168, 129–136, doi:10.3189/172756504781830330,



- 2004a.
- Haeberli, W., Huggel, C., Kääh, A., Zraggen-Oswald, S., Polkvoj, A., Galushkin, I., Zotikov, I., and Osokin, N.: The Kolka-Karmadon rock/ice slide of 20 September 2002: An extraordinary event of historical dimensions in North Ossetia, Russian Caucasus, *J. Glaciol.*, 50, 171, 533–546, doi:10.3189/172756504781829710, 2004b.
- 915 Haeberli, W., Schaub, Y. and Huggel, C.: Increasing risks related to landslides from degrading permafrost into new lakes in de-glaciating mountain ranges. *Geomorphology* 293, 405–417. doi:10.1016/j.geomorph.2016.02.009, 2017
- Haeberli, W., Wegmann, M., and Vonder Mühl, D.: Slope stability problems related to glacier shrinkage and permafrost degradation in the Alps, *Eclogae Geol. Helv.*, 90, 407–414, 1997.
- Hess, H.: Leo Handl's Temperatur-Messungen des Eises und der Luft in den Stollen des Marmolata-Gletschers und denen
920 des Ortlergebietes, *Z. Gletscherkd.*, 27, 1–2, 168–171, 1940.
- Hock, R., Bliss, A., Giesen, R., Marzeion, B., Hirabayashi, Y., Huss, M., Radic, V., and Slangen, A.: GlacierMIP - A model intercomparison of global-scale glacier mass-balance models and projections, *J. Glaciol.*, 65, 251, 453–467, doi:10.1017/jog.2019.22, 2019.
- Hooke, R. L. B., and Hudleston, P.: Origin of foliation in glaciers, *J. Glaciol.*, 20, 285–299,
925 doi:10.3189/S0022143000013848, 1978.
- Huang, D., Meng, Q., Songa, Y., Guc, D., Cend, D., and Zhong, Z.: Experimental study on the shear mechanical behavior of ice-rich debris–rock interface: effects of temperature, stress, and ice content, *Can. Geotech. J.*, 61, 1051–1072, doi:10.1139/cgj-2023-0375, 2024.
- Huggel, C., Kääh, A., Haeberli, W., Teyssie, P., and Paul, F.: Remote sensing-based assessment of hazards from glacier
930 lake outbursts: A case study in the Swiss Alps, *Can. Geotech. J.*, 39, 2, 316–330, 2002.
- Hutter, K.: Snow and Glacier Rheology, *Appl. Rheol.*, 7, 6, 266–276, doi:10.3933/ApplRheol-7-266, 1997.
- Irvine-Fynn, T. D. L., Hodson, A. J., Moorman, B. J., Vatne, G., and Hubbard, A. L.: Polythermal glacier hydrology: a review, *Rev. Geophys.*, 49, RG4002, doi:10.3189/172756501781831972, 2011.
- Janbu, N.: Application of composite slip surface for stability analysis, *Proceedings of European conference on stability of
935 earth slopes*, Stockholm, 3, 43–49, 1954.
- Janbu, N., Bjerrum, L., and Kjaernsli, B.: Soil mechanics applied to some engineering problems, *Norwegian Geotechnical Institute Publication* 16, Oslo, Norway, 1956.
- Janbu, N.: Slope stability computations, in: *Embankment Dam Engineering, Casagrande Memorial Volume* (eds E. Hirschfeld and S. Poulos), 47–86, New York, Wiley, 1973.
- 940 Jennings, S. J. A., and Hambrey, M. J.: Structures and deformation in glaciers and ice sheets, *Rev. Geophys.*, 59, e2021RG000743, doi:10.1029/2021RG000743, 2021.
- Jouvet, G., Picasso, M., Rappaz, J., Huss, M., and Funk, M.: Modelling and Numerical Simulation of the Dynamics of Glaciers Including Local Damage Effects, *Math. Model. Nat. Phenom.*, 6, 5, 263–280, doi:10.1051/mmnp/20116510, 2011.



- Kargel, J. S., Leonard, G. J., Shugar, D. H., Haritashya, U. K., Bevington, A., Fielding, E. J., Fujita, K., Geertsema, M.,
945 Miles, E. S., Steiner, J., and Anderson, E.: Geomorphic and geologic controls of geohazards induced by Nepal's 2015
Gorkha earthquake, *Science*, 351, 6269, aac8353, 2016.
- Kavanaugh, J. L., and Clarke, G. K. C.: Abrupt glacier motion and reorganisation of basal shear stress following the
establishment of a connected drainage system, *J. Glaciol.*, 47, 158, 472–480, doi:10.3189/172756501781831972, 2001.
- Lee W. H., and Lahr, J. C.: Hypo71 (revised): a computer program for determining local earthquake hypocentral parameters,
950 magnitude, and first motion pattern of local earthquakes, US Geol. Survey Open-file Report 75-311, doi:10.3133/ofr75311,
1975.
- Löfgren, A., Zwinger, T., Råback, P., Helanow, C., and Ahlkrona, J.: Increasing numerical stability of mountain valley
glacier simulations: implementation and testing of free-surface stabilization in Elmer/Ice, *EGUsphere*,
doi:10.5194/egusphere-2023-1507, 2023.
- 955 Logan, L. C., Lavier, L. L., Choi, E., Tan, E., and Catania, G. A.: Semi-brittle rheology and ice dynamics in DynEarthSol3D,
Cryosphere, 11, 1, 117–132, doi:10.5194/tc-11-117-2017, 2017.
- Lomax, A., Satriano, C., and Vassallo, M.: Automatic picker developments and optimization: FilterPicker--a robust,
broadband picker for real-time seismic monitoring and earthquake early warning, *Seismological Research Letters*, 83, 3,
531–540, doi:10.1785/gssrl.83.3.531, 2012.
- 960 Longo, E.: La determinazione della resistenza a compressione uniassiale nelle rocce: un confronto tra i principali metodi
applicati alla serie dolomitica, MSc Thesis, University of Padova, 133 pp., 2018.
- Lützow, N., Veh, G., and Korup, O.: A global database of historic glacier lake outburst floods, *Earth Syst. Sci. Data*, 15,
2983–3000, doi:10.5194/essd-15-2983-2023, 2023.
- Madhukar, B. N. and Narendra, R.: Lanczos Resampling for the Digital Processing of Remotely Sensed Images, *Proceedings*
965 *of VCASAN-2013, Lecture Notes in Electrical Engineering*, Springer, 258, 403–411, 2013.
- Margreth, S., Failletaz, J., Funk, M., Vagliasindi, M., Diotri, F., and Broccolato, M.: Safety concept for hazards caused by
ice avalanches from the Whympfer hanging glacier in the Mont Blanc Massif, *Cold Reg. Sci. Technol.*, 69, 194–201, 2011.
- Margreth, S., Funk, M., Tobler, D., Dalban, P., Meier, L., and Lauper, J.: Analysis of the hazard caused by ice avalanches
from the hanging glacier on the Eiger west face, *Cold Reg. Sci. Technol.*, 144, 63–72,
970 doi:10.1016/j.coldregions.2017.05.012, 2017.
- Marta, S., Azzoni, R. S., Fugazza, D., Tielidze, L., Chand, P., Sieron, K., Almond, P., Ambrosini, R., Anthelme, F., Alviz
Gazitúa, P., et al.: The Retreat of Mountain Glaciers since the Little Ice Age: A Spatially Explicit Database, *Data*, 6, 107,
doi:10.3390/data6100107, 2021.
- Marzeion, B., Hock, R., Anderson, B., Bliss, A., Champollion, N., Fujita, K., et al.: Partitioning the uncertainty of ensemble
975 projections of global glacier mass change, *Earth's Future*, 8, e2019EF001470, doi:10.1029/2019EF001470, 2020.
- McFeeters, S. K.: The use of the Normalized Difference Water Index (NDWI) in the delineation of open water features,
International Journal of Remote Sensing, 17, 7, 1425–1432, 2016.



- Mikesell, T., van Wijk, K., Haney, M. M., Bradford, J. H., Marshall, H.-P., and Harper, J. T.: Monitoring glacier surface seismicity in time and space using Rayleigh waves, *J. Geophys. Res.: Earth Surf.*, 117, F2, doi:10.1029/2011JF002259, 980 2012.
- Mortara, G., and Dutto, F.: A case of sudden evolution of Monviso glaciers: the ice avalanche of Upper Coolidge Glacier, *Geogr. Fis. Dinam. Quat.*, 13, 187–189, 1990.
- Morgenstern, N. R., and Price, V.E.: The analysis of the stability of general slip surfaces, *Geotechnique*, 15, 1, 79–93, 1965.
- Noetzli, J., and Gruber, S., 2009, Transient thermal effects in Alpine permafrost, *The Cryosphere*, 3, 85–99, doi:10.5194/tc-985 3-85-2009.
- Noetzli, J., Gruber, S., Kohl, T., Salzmann, N., and Haerberli, W.: Three-dimensional distribution and evolution of permafrost temperatures in idealized high-mountain topography, *J. Geophys. Res.*, 112, F02S13, doi:10.1029/2006JF000545, 2007.
- Noetzli, J., Huggel, C., Hoelzle, M., and Haerberli, W.: GIS-based modelling of rock-ice avalanches from Alpine permafrost areas, *Comput. Geosci.*, 10, 161–178, doi:10.1007/s10596-005-9017-z, 2006.
- 990 Olivieri, L., and Bettanini, C.: Preliminary observation of Marmolada glacier collapse of July 2022 with space-based cameras, *Remote Sens. Lett.*, 14, 1, 21–29, doi:10.1080/2150704X.2022.2152754, 2022.
- Pasta, M., 2004, Esecuzione ed interpretazione di misure georadar sul ghiacciaio della Marmolada e studi di fattibilità su ghiacciai del Fradusta e dell'Antelao Superiore, Università di Genova, DipTeRis, Technical Report, 20 pp.
- Pasta, M., Pavan, M., Sonda, D., Carollo, F., and Cagnati, A.: Prospezione di alcuni ghiacciai dolomitici tramite tecniche 995 GPR e GPS, *Neve e Valanghe*, 56, 50–59, 2005.
- Pasta, M.: Esecuzione ed interpretazione di misure georadar sul ghiacciaio della Marmolada e studi di fattibilità su ghiacciai del Fradusta e dell'Antelao Superiore, Univ. Genova, DipTeRis, Technical Report, 20 pp., 2004.
- Paterson, W. S. B.: *The Physics of Glaciers*, 3rd ed., Pergamon, Oxford, U.K., 480 pp., ISBN-13: 9780080379457, 1994.
- Paul, F., Kääh, A., Maisch, M., Kellenberger, T., and Haerberli, W.: Rapid disintegration of Alpine glaciers observed with 1000 satellite data, *Geophys. Res. Lett.*, 31, 21, L21402, 1–4, doi:10.1029/2004GL020816, 2004.
- Pelto, M., WGMS Network: Alpine glaciers, in *State of the Climate in 2019*, *Bull. Am. Meteorol. Soc.*, 101, 8, S37–S38, doi:10.1175/2020BAMSStateoftheClimate.1, 2020
- Pettenati, F., Maharjan, D. K., Paudyal, S., Sandron, D., Wagle, S., Cravos, C., Giorgi, M., and Shrestha, S. N.: Structure of the Kathmandu basin inferred from microtremor measurements: a preliminary study, *Geophys. J. Int.*, 1–16, 1005 doi:10.1093/gji/ggac465, 2023.
- Picotti, S., Francese, R., Giorgi, M., Pettenati, F., and Carcione, J. M.: Estimation of glaciers thicknesses and basal properties using the horizontal-to-vertical component spectral ratio (HVSR) technique from passive seismic data, *J. Glaciol.*, 63, 229–248, doi:10.1017/jog.2016.135, 2017.
- Podolskiy, E. A., Nishimura, K., Abe, O., and Chernous, P. A.: Earthquake-induced snow avalanches: I. Historical case 1010 studies, *J. Glaciol.*, 56, 197, 431–446, doi:10.3189/002214310792447815, 2010.



- Pralong, A., and Funk, M.: On the instability of avalanching glaciers, *J. Glaciol.*, 52, 176, 31–48, doi:10.3189/172756506781828980, 2006.
- Pralong, A., Birrer, C., Stahel, W. A., and Funk, M.: On the predictability of ice avalanches, *Nonlinear Process. Geophys.*, 12, 849–861, doi:10.5194/npg-12-849-2005, 2005.
- 1015 Rebez, A., Renner, G., Sandron, D., and Slejko, D.: The eastern Alps earthquake catalogue (1977–2022), *Bull. Geophys. Oceanogr.*, 65, 1, 115–122, doi:10.4430/bgo00453, 2024.
- Richards, K., Sharp, M., Arnold, N., Gurnell, A., Clark, M., Tranter, M., Nienow, P., Brown, G., Willis, I., and Lawson, W.: An integrated approach to modeling hydrology and water quality in glacierized catchments, *Hydrol. Process.*, 10, 4, 479–508, 1996.
- 1020 Rossi, M., Dal Cin, M., Picotti, S., Gei, D., Isaev, V. S., Pogorelov, A. V., Gorshkov, E. I., Sergeev, D. O., Kotov, P. I., Giorgi, M., and Rainone, M. L.: Active Layer and Permafrost Investigations Using Geophysical and Geocryological Methods - A Case Study of the Khanovey Area, Near Vorkuta, in the NE European Russian Arctic, *Front. Earth Sci.*, 10, 910078, doi:10.3389/feart.2022.910078, 2022.
- Röthlisberger, H., and Lang, H.: Glacial hydrology, in *Glacio-Fluvial Sediment Transfer: An Alpine Perspective*, edited by A.M. Gurnell and M.J. Clark, John Wiley, Chichester, U.K., 207–284, 1987.
- 1025 Röthlisberger, H.: Eislawinen und Ausbrüche von Gletscherseen, in Kasser, P., ed., *Gletscher und Klima – glaciers et climat*, Jahrbuch der Schweizerischen Naturforschenden Gesellschaft, wissenschaftlicher Teil 1978. Basel, Birkhäuser Verlag, 170–212, 1981.
- Rounce, D. R., Hock, R., Maussion, F., Hugonnet, R., Kochtitzky, W., Huss, M., Berthier, E., Brinkerhoff, D., Compagno, L., Copland, L., Farinotti, D., Menounos, B., and McNabb, R. W.: Global glacier change in the 21st century: Every increase in temperature matters, *Science*, 379, 6627, 78–83, doi:10.1126/science.abo1324, 2023.
- 1030 Ruols, B., Baron, L., and Irving, J.: Development of a drone-based ground penetrating radar system for efficient and safe 3D and 4D surveying of alpine glaciers, *J. Glaciol.*, 1–12, doi:10.1017/jog.2023.83, 2023.
- Saeki, H., Ono, T., En Zong, N., and Nakazawa, N.: Experimental study on direct shear strength of sea ice, *Ann. Glaciol.*, 6, 1035 1, 218–221, 1985.
- Saim, N. M., and Kasa, A.: Comparative Analysis of Slope Stability using Finite Element Method (FEM) and Limit Equilibrium Method (LEM), 2023 IEEE 14th Control and System Graduate Research Colloquium, ICSGRC 2023 - Conference Proceeding, 224–229, doi:10.1109/ICSGRC57744.2023.10215453, 2023.
- Santin, I., Colucci, R., Žebre, M., Pavan, M., Cagnati, A., and Forte, E.: Recent evolution of Marmolada glacier (Dolomites, Italy) by means of ground and airborne GPR surveys, *Remote Sens. Environ.*, 235, 111442, 2019.
- 1040 SAT – Società Alpinistica Tridentina, Commissione Glaciologica: Marmolada, le immagini del ghiacciaio dal drone il giorno prima della valanga - UAV video of the marmolada glacier taken the day before the ice-avalanche, accessed Jul. 4, 2022, https://www.youtube.com/watch?v=QkpvW4L1WJ4&-ab_channel=CorrieredellaSera.
- Smiraglia, C., and Diolaiuti, G., *The New Italian Glacier Inventory*, EVK2CNR, 395 pp., ISBN unavailable, 2016.



- 1045 Stearns, L. A., and Van Der Veen, C. J.: Friction at the bed does not control fast glacier flow, *Science*, 361, 6399, 273–277, doi:10.1126/science.aat2217, 2018.
- Stockwell, J. W., Jr.: Free software in education: a case study of CWP/SU: Seismic Unix, *Leading Edge*, 61, 3, 759–775, 1999.
- Sugan, M., and Peruzza, L.: Distretti sismici del Veneto, *Boll. Geofis. Teor. Appl.*, 52, Suppl., s3–s90, 2011.
- 1050 Sugan, M., Kato, A., Miyake, H., Nakagawa, S., and Vuan, A.: The preparatory phase of the 2009 Mw 6.3 L'Aquila earthquake by improving the detection capability of low-magnitude foreshocks, *Geophys. Res. Lett.*, 41, 17, 6137–6144, 2014.
- Suter, S., Laternser, M., Haeberli, W., Frauenfelder, R., and Hoelzle, M.: Cold firn and ice of high-altitude glaciers in the Alps: measurements and distribution modeling, *J. Glaciol.*, 45, 156, 85–96, 2001.
- 1055 Tang, M., Zhao, H., Xu, Q., Ni, W., Li, G., Zuo, Z., Chen, X., Zhong Y.: Experimental study on the shear strength and failure mechanism of mountain glacier ice, *Natural Hazards and Earth System Sciences*, EGUsphere, preprint, <https://doi.org/10.5194/egusphere-2024-1522>, 2024.
- Thibert, E., Faug, T., Naaim, M., Bonnefoy-Demongeot, M., Gilbert, A., Vincent, C., Gagliardini, O., and Funk, M.: Retrieving Ice-avalanche basal friction law parameters from a back-analysis of the collapse of Altels glacier (1895, Bernese
- 1060 Alps, Switzerland). Application to Taconnaz glacier instability (French Alps), *Int. Snow Sci. Workshop*, Innsbruck, Austria, 66–70, 2018.
- Tian, L., Yao, T., Gao, Y., Thompson, L., Mosley-Thompson, E., Muhammad, S., Zong, J., Wang, C., Jin, S., and Li, Z.: Two glaciers collapse in western Tibet, *J. Glaciol.*, 63, 194–197, doi:10.1017/jog.2016.122, 2017.
- Viani, C., Chiarle, M., Paranunzio, R., Merlone, A., Musacchio, C., Coppa, G., and Nigrelli, G.: An integrated approach to
- 1065 investigate climate-driven rockfall occurrence in high alpine slopes: the Bessanese glacial basin, Western Italian Alps, *J. Mt. Sci.*, 17, 2591–2610, doi:10.1007/s11629-020-6216-y, 2020.
- Vincent, C., Thibert, E., Harter, M., Soruco, A., and Gilbert, A.: Volume and frequency of ice avalanches from Taconnaz hanging glacier, French Alps, *Ann. Glaciol.*, 56, 70, doi:10.3189/2015AoG70A017, 2015.
- Walter, F., Clinton, J. F., Deichmann, N., Dreger, D. S., Minson, S. E., and Funk, M.: Moment tensor inversions of
- 1070 icequakes on Gornergletscher, Switzerland, *Bull. Seismol. Soc. Am.*, 99, 2A, 852–870, 2009.
- Wilson, N. J., and Flowers, G.: Environmental controls on the thermal structure of alpine glaciers, *Cryosphere*, 7, 167–182, doi:10.5194/tc-7-167-2013, 2013.
- Zekollari, H., Huss, M., Farinotti, D., and Lhermitte, S.: Ice-dynamical glacier evolution modeling—A review, *Rev. Geophys.*, 60, e2021RG000754, doi:10.1029/2021RG000754, 2022.
- 1075 Zemp, M., Frey, H., Gärtner-Roer, I., Nussbaumer, S. U., Hoelzle, M., Paul, F., et al.: Historically unprecedented global glacier decline in the early 21st century, *J. Glaciol.*, 61, 228, doi:10.3189/2015JoG15J017, 2015.
- Zemp, M., Huss, M., Thibert, E., et al.: Global glacier mass changes and their contributions to sea-level rise from 1961 to 2016, *Nature*, 568, 382–386, doi:10.1038/s41586-019-1071-0, 2019.



Zhao, C., Yang, W., Westoby, M., An, B., Wu, G., Wang, W., Wang, Z., Wang, Y., and Dunning, S.: An approximately 50
1080 Mm³ ice-rock avalanche on 22 March 2021 in the Sedongpu valley, southeastern Tibetan Plateau, *Cryosphere*, 16, 1333–
1340, doi:10.5194/tc-16-1333-2022, 2022.

Zhao, L., Yang, Y., Cheng, W., Ji, D., and Moore, J. C.: Glacier evolution in high-mountain Asia under stratospheric sulfate
aerosol injection geoengineering, *Atmos. Chem. Phys.*, 17, 6547–6564, doi:10.5194/acp-17-6547-2017, 2017.